J. Fluid Mech. (1990), *vol.* 217, *pp.* 1–32
Printed in Great Britain

Centrifugal instability of an oscillatory flow over periodic ripples

By TETSU HARA AND CHIANG C. MEI
Department of Civil Engineering, Massachusetts Institute of Technology, Cambridge, MA 02139, USA

(Received 8 May 1989 and in revised form 12 September 1989)

An oscillating flow over a sandy beach can initiate and enhance the formation of bed ripples, with crests perpendicular to the direction of the ambient oscillation. Under certain circumstances, bridges may develop to span adjacent ripple crests, resulting in a brick pattern. It has been suggested that the onset of this transition is due to a three-dimensional centrifugal instability of an otherwise two-dimensional flow over periodic long-crested ripples. Here we analyse theoretically such an instability by assuming that the ripples are rigid and smooth. Two complementary cases are studied. We first consider a weak ambient oscillation over ripples of finite slope in Case (i). The three-dimensional disturbance is found to be localized in a small region either along the crests or along the troughs. In Case (ii) we analyse finite oscillations over ripples of mild slope. The region influenced by the instability is now comparable with a ripple wavelength and the unstable disturbance along adjacent ripples may interact with each other. Four types of harmonic and subharmonic instabilities are found. The associated steady streaming close to the ripple surface shows various tendencies of possible sand accumulations, some of which appear to be qualitatively relevant to the initiation of brick-patterned ripples.

1. Introduction

When water waves travel over a sandy beach, the oscillatory flow close to the bed interacts with sand particles and often enhances the formation of ripples. In water of depth O(2–10 m), the typical scale of these ripples is of O(10 cm) whereas the surface wavelength is of O(10–100 m). Therefore for the dynamics over the ripples, the effects of the free surface and breaking can be quite negligible except in the swash and surf zones, and the ambient forcing is essentially a pure oscillatory flow. Bagnold (1946) was the first to investigate this mechanism experimentally, by oscillating at various amplitudes a section of sand bed in still water. When the relative speed exceeds a critical value at which sand particles begin to move along the bed, rolling-grain ripples are first formed with crests perpendicular to the direction of the ambient flow. The slope of these ripples is so small that the flow does not separate behind the crests. If the water speed exceeds about twice the critical speed, vortex ripples will appear instead, which are steep enough to induce vortices behind the crests. Vortex ripples can also form at a lower water speed from any obstacle protruding above the initially flat sand surface. When the oscillation amplitude A is reduced to about one-sixth of the ripple wavelength λ these originally two-dimensional vortex ripples are transformed to a brick-like pattern. More thorough investigations of the formation of ripples including those of brick pattern have been conducted by Sleath & Ellis (1978). They oscillated a tray with an initially uniform

layer of sediment in a tank of still water, and measured the bed geometry when it reached an equilibrium state. Three kinds of particles were used and different oscillation amplitudes and frequencies were examined. Based on these experiments, Sleath (1984) has suggested that brick-patterned ripples occur when the orbital amplitude A is less than $\frac{1}{2}\lambda_0$, where λ_0 is the maximum wavelength of the two-dimensional vortex ripples for a given oscillation frequency and sand properties. By assuming that the three-dimensional ripples are already present, he has further suggested that horseshoe vortices may form between adjacent bridges in the lee of the transverse crests, and tend to move sand particles towards the bridges as well as towards the transverse crests, thereby enhancing further growth of the brick pattern. While this mechanism may be relevant to the later stage of growth toward equilibrium, it does not explain the initial appearance of such three-dimensional topography which is most likely started by some instability mechanism.

The simplest instability problem of an oscillatory flow is the two-dimensional case above a flat surface. Kerczek & Davis (1974) have given a linearized analysis of the two-dimensional instability of the oscillatory Stokes layer in a fluid of finite but large depth h between two parallel plates, and predicted absolute stability for $Re = \sqrt{2}A\omega\delta/\nu < 800$ if $\beta = h/\sqrt{2}\delta = 8$ (where $\delta = (\nu/\omega)^{\frac{1}{2}}$ is the viscous boundary-layer thickness, ν is the viscosity of water, and ω is the angular frequency). On the other hand, experiments by Li (1954) for $\beta > 175$ suggest that the transition to turbulence occurs around $Re \approx 566$, while experiments by Sergeev (1966) for $\beta > 3.5$ give a lower threshold, $Re \approx 495$. The instability of a viscous fluid on an oscillating plate with a free surface without waves in the basic state has been investigated by Yih (1968) for $0.1 < \beta < 10$. An extensive survey of the linear two-dimensional instability of time-periodic flows, including unidirectional flow (oscillation plus a current) and centrifugal instability between concentric cylinders, has been given by Davis (1976).

Developments on the instability of external oscillatory flows around a curved surface are relatively recent. In particular, Honji (1981) oscillated transversely a circular cylinder of radius R in still water, and visualized the flow around the cylinder by using the smoke of metallic compounds. When the oscillation amplitude A exceeds a certain threshold for a given frequency, smoke streaks are formed at regular spacings along the cylinder. In every oscillation mushroom-shaped vortices are first shed from the cylinder surface, at the same spacing, along the crowns, i.e. the two lines where the ambient fluid velocity is maximum. These vortices are then convected in the direction of oscillation and help to form the equally spaced streaks. This three-dimensional structure disappears when A is beyond a second threshold, whereupon the flow becomes turbulent. Honji plotted these two thresholds as curves of A/R versus the 'Stokes number' ($St = (2/\pi)(R/\delta)^2$), for the range of $70 < St < 700$. This spanwise instability was later theoretically explained by Hall (1984). Assuming that A/R and δ/A are both small but the Taylor number $T \sim A^2/R\delta$ is of order unity, he has shown that an instability of centrifugal type can occur when T exceeds a certain threshold. The theoretical value of this threshold is found to be in good agreement with Honji's experiment. Physically, this instability takes place inside the thin viscous boundary layer and is localized near the point where the ambient velocity is maximum. Hall's theory can be generalized for an oscillatory flow over other convex surfaces; the threshold of instability is always governed by the local Taylor number $T_L \sim A_L^2/R_L\delta$, where A_L is the local amplitude of the oscillation, and R_L is the local radius of curvature. In addition, Hall extended the theory to a higher order in δ/R by accounting for nonlinear effects, and obtained the spatial dependence of the unstable mode amplitude along the circumference of the cylinder.

In an experimental study of the forces on a circular cylinder of smooth or rough surface in a viscous oscillatory flow, Sarpkaya (1986) also observed Honji's instability for a wider range of Stokes number, and confirmed Hall's theoretical prediction up to $St < 5500$.

In acoustics, Thompson (1987) has investigated theoretically sound waves in a two-dimensional waveguide with rigid wavy walls. For large H/δ, where H is the distance between the walls, he has shown that a similar mechanism of centrigugal instability may take place also.

Direct evidence of the relevance of centrifugal instability to the formation of brick-like ripples was first found in the exploratory experiments by Matsunaga & Honji (1980) who used a periodic array of parallel half-circular cylinders attached on a flat plate. In the first experiment this two-dimensional ripple model was oscillated in still water with a relatively small amplitude ($\alpha = A/\lambda = 0.28$). Regularly spaced streaks were observed along the crests as in the case of a single cylinder. The positions of streaks on adjacent cylinders were found to be out of phase by half the streak intervals. In the second experiment, an array of half-cylinders was placed on the bottom of a water tunnel, and glass beads were spread between the crests. When water was forced to oscillate with a large amplitude ($\alpha = 0.60$), the glass beads began to drift in the troughs between the cylinders, and finally formed brick-patterned accumulations. These observations clearly show that the two-dimensional flow over ripples can be unstable to three-dimensional disturbances, and suggest that the unstable mode can be subharmonic. The observed subharmonic structure also indicates that the disturbance along one ripple is not localized, but interacts with those along adjacent ripples. This is quite different from the case of a single cylinder, where the disturbance is confined in a narrow region around the two crowns of the cylinder.

In this paper we present a quantitative theory of centrifugal instability in a two-dimensional laminar oscillatory flow over periodic rigid ripples, with a view to examining its possible relevance to the initiation of brick-pattern sandy ripples. Many theoretical papers on the two-dimensional basic flows exist. First among these is the work of Lyne (1971) who gave a perturbation analysis for small a/δ (a is the ripple amplitude) suitable for high viscosity or low frequency. He obtained not only the Stokes layer at the first order, but also the induced streaming at the next order. Extensions along the same lines have been obtained by Kaneko & Honji (1979) and Vittori (1989). The present authors have recently examined a broad range of a/δ including $a/\delta \geqslant O(1)$ (Hara & Mei 1990). Specifically, we considered two cases with different small parameters: Case (i) weak oscillations over ripples of finite slope: $\alpha = A/\lambda \ll 1$ but $\epsilon = a/\lambda = O(1)$; Case (ii) moderate oscillations over very gentle ripples: $\epsilon \ll 1$ but finite α. In both cases viscous effects and convective inertia are important within a rather thick layer of $O(\delta/\alpha)$ and $O(\delta/\epsilon^{\frac{1}{2}})$, respectively, above the ripple surface. Nevertheless, the Stokes layer is still preserved at the first order near the ripple surface where the instantaneous acceleration balances the viscous stress. In this paper we focus on the instability within the Stokes layer for these two cases. In Case (i) the disturbance is localized in a small region along one ripple, and the analysis closely follows that by Hall. The threshold of the instability is given in terms of the local Taylor number. In contrast to a circular cylinder, however, the instability may also occur along the troughs where the radius of curvature is negative.

Our principal results are for Case (ii) where the oscillation amplitude is finite but the ripple slope is so small that there is no separation in the basic flow. The region

influenced by the instability is now comparable with a ripple wavelength and the disturbance along one ripple may interact with those along adjacent ripples. The unstable flow is either harmonic (periodic within one wavelength of ripples) or subharmonic (periodic within twice the wavelength of ripples) depending on the mode of instability. The associated steady streaming along the ripple surface shows a tendency that would accumulate sand particles in various patterns, including one suggesting the initiation of the brick-patterned ripples. The consistency between the results in Case (i) and Case (ii) is shown. Finally, the experiments with rigid cylinders by Matsunaga & Honji (1980), and those with sand ripples by Sleath & Ellis (1978) are discussed. Since in these experiments vortex shedding is likely to be present in the basic flow, only qualitative comparisons can be made, which nevertheless suggest that centrifugal instability can be a part of the mechanism of brick-like ripples. Satisfactory confirmation awaits extension of the theory and the experiments.

2. Equations in curvilinear coordinates

We consider the flow of an incompressible viscous fluid above a periodically rippled surface which is rigid and smooth. Referring to figure 1, the ambient fluid oscillates in the x-direction transverse to the ripple crests. As a reference, we first define the usual rectilinear coordinates with y pointing vertically upwards, x normal and z parallel to the ripple crests, as shown in figure 1. The governing equations will however be written in terms of the orthogonal coordinates ξ and η which are related to x and y by the conformal transformation (Benjamin 1959; Lyne 1971):

$$\left.\begin{aligned} x &= \xi - a\exp\left(-\frac{2\pi\eta}{\lambda}\right)\sin\frac{2\pi\xi}{\lambda}, \\ y &= \eta + a\exp\left(-\frac{2\pi\eta}{\lambda}\right)\cos\frac{2\pi\xi}{\lambda}, \end{aligned}\right\} \tag{2.1}$$

where a is a measure of the amplitude and λ is the wavelength of the ripples. In the ξ, η, z system, the ripple surface is given by $\eta = 0$; the fluid above a ripple period in the (x, y)-plane maps onto the rectangular semi-infinite strip $\eta > 0$, $0 < \xi/\lambda < 1$. The Jacobian of transformation is

$$J = 1 - 2\left(\frac{2\pi a}{\lambda}\right)\exp\left(-\frac{2\pi\eta}{\lambda}\right)\cos\frac{2\pi\xi}{\lambda} + \left(\frac{2\pi a}{\lambda}\right)^2\exp\left(-\frac{4\pi\eta}{\lambda}\right). \tag{2.2}$$

We define (u, v, w) to be the velocity components in (ξ, η, z) directions. Let us introduce the following normalization which is appropriate for the Stokes boundary layer:

$$\left.\begin{aligned} u' = \frac{u}{A\omega}, \quad v' = \frac{u}{A\omega\delta/\lambda}, \quad w' = \frac{w}{A\omega\delta/\lambda}, \quad p' = \frac{p}{\rho A\omega^2\lambda}, \\ \xi' = \frac{\xi}{\lambda}, \quad \eta' = \frac{\eta}{\delta}, \quad z' = \frac{z}{\delta}, \quad t' = \omega t, \end{aligned}\right\} \tag{2.3}$$

where $\delta = (\nu/\omega)^{\frac{1}{2}}$ is the Stokes boundary-layer thickness. A and ω are the amplitude and the frequency of the ambient oscillation. Note that the scales in the z-direction are chosen to be the same as in the y-direction, as suggested by the work of Hall. For

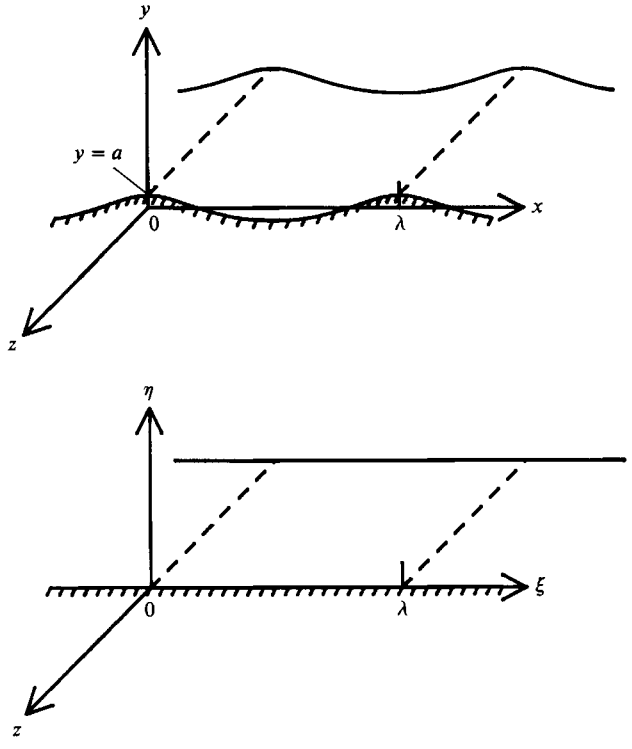

FIGURE 1. Definitions of (x, y, z) and (ξ, η, z) coordinate systems.

brevity we shall also omit the primes from here on. From their forms in the general orthogonal curvilinear system (see e.g. Batchelor 1967, p. 598 ff), the normalized Navier–Stokes equations in the ξ-, η- and z-coordinates can be deduced:

$$\frac{\partial(J^{\frac{1}{2}}u)}{\partial\xi}+\frac{\partial(J^{\frac{1}{2}}v)}{\partial\eta}+J\frac{\partial w}{\partial z}=0, \tag{2.4}$$

$$\begin{aligned}&\frac{\partial u}{\partial t}+\alpha\left(u\frac{1}{J^{\frac{1}{2}}}\frac{\partial u}{\partial\xi}+v\frac{1}{J^{\frac{1}{2}}}\frac{\partial u}{\partial\eta}+w\frac{\partial u}{\partial z}+\frac{uv}{J}\frac{\partial J^{\frac{1}{2}}}{\partial\eta}\right)-\alpha\sigma^2\frac{v^2}{J}\frac{\partial J^{\frac{1}{2}}}{\partial\xi}\\&\quad=-\frac{1}{J^{\frac{1}{2}}}\frac{\partial p}{\partial\xi}-\sigma^2\frac{1}{J^{\frac{1}{2}}}\frac{\partial}{\partial\eta}\left[\frac{1}{J}\frac{\partial(J^{\frac{1}{2}}v)}{\partial\xi}\right]-\frac{1}{J^{\frac{1}{2}}}\frac{\partial}{\partial\eta}\left[-\frac{1}{J}\frac{\partial(J^{\frac{1}{2}}u)}{\partial\eta}\right]\\&\qquad+\frac{1}{J^{\frac{1}{2}}}\frac{\partial}{\partial z}\left[J^{\frac{1}{2}}\frac{\partial u}{\partial z}\right]+\sigma^2\frac{1}{J^{\frac{1}{2}}}\frac{\partial}{\partial z}\left[-\frac{\partial w}{\partial\xi}\right],\end{aligned} \tag{2.5}$$

$$\begin{aligned}&\frac{\partial v}{\partial t}+\alpha\left(u\frac{1}{J^{\frac{1}{2}}}\frac{\partial v}{\partial\xi}+v\frac{1}{J^{\frac{1}{2}}}\frac{\partial v}{\partial\eta}+w\frac{\partial v}{\partial z}+\frac{uv}{J}\frac{\partial J^{\frac{1}{2}}}{\partial\xi}\right)-\alpha\frac{1}{\sigma^2}\frac{u^2}{J}\frac{\partial J^{\frac{1}{2}}}{\partial\eta}\\&\quad=-\frac{1}{\sigma^2}\frac{1}{J^{\frac{1}{2}}}\frac{\partial p}{\partial\eta}-\frac{1}{J^{\frac{1}{2}}}\frac{\partial}{\partial z}\left[\frac{\partial w}{\partial\eta}-J^{\frac{1}{2}}\frac{\partial v}{\partial z}\right]+\sigma^2\frac{1}{J^{\frac{1}{2}}}\frac{\partial}{\partial\xi}\left[\frac{1}{J}\frac{\partial(J^{\frac{1}{2}}v)}{\partial\xi}\right]\\&\qquad-\frac{1}{J^{\frac{1}{2}}}\frac{\partial}{\partial\xi}\left[\frac{1}{J}\frac{\partial(J^{\frac{1}{2}}u)}{\partial\eta}\right],\end{aligned} \tag{2.6}$$

$$\frac{\partial w}{\partial t}+\alpha\left(u\frac{1}{J^{\frac{1}{2}}}\frac{\partial w}{\partial \xi}+v\frac{1}{J^{\frac{1}{2}}}\frac{\partial w}{\partial \eta}+w\frac{\partial w}{\partial z}\right)$$

$$=-\frac{1}{\sigma^2}\frac{\partial p}{\partial z}-\frac{1}{J}\frac{\partial}{\partial \xi}\left[J^{\frac{1}{2}}\frac{\partial u}{\partial z}\right]-\sigma^2\frac{1}{J}\frac{\partial}{\partial \xi}\left[-\frac{\partial w}{\partial \xi}\right]+\frac{1}{J}\frac{\partial}{\partial \eta}\left[\frac{\partial w}{\partial \eta}-J^{\frac{1}{2}}\frac{\partial v}{\partial z}\right], \quad (2.7)$$

while the dimensionless Jacobian is

$$J=1-4\pi\epsilon\cos(2\pi\xi)\,\mathrm{e}^{-2\pi\sigma\eta}+4\pi^2\epsilon^2\,\mathrm{e}^{-4\pi\sigma\eta}. \quad (2.8)$$

Use has been made of the fact that $h_1=h_2=J^{\frac{1}{2}}, h_3=1$ where (h_1,h_2,h_3) are the standard scale factors in (ξ,η,z)-directions. Three dimensionless parameters appear in these equations: $\epsilon=a/\lambda=$ ripple slope; $\alpha=A/\lambda=$ amplitude of ambient oscillations relative to the ripple wavelength; $\sigma=\delta/\lambda=$ boundary-layer thickness relative to the ripple wavelength. We only consider small viscosity so that $\sigma\ll 1$.

In the case of a single cylinder in a weakly oscillating flow, Hall found that the instability occurs when the Taylor number

$$T=O(A^2/\delta R), \quad (2.9)$$

which measures the ratio of the centrifugal force to the viscous stress, exceeds a certain critical value of order unity, with the auxiliary conditions that

$$\frac{A}{R}\sim\frac{\delta}{A}\ll 1. \quad (2.10)$$

This Taylor number has local maxima when the local inviscid velocity is the greatest, i.e. at two crowns of the cylinder along the diameter normal to the ambient oscillations, and the unstable disturbances are localized near these crowns. Now for periodic ripples, described by (2.1) with $\eta=0$, the maximum local radius of the curvature is of the order $R=O(\lambda^2/a)$. Thus the Taylor number can be defined as

$$T=\frac{A^2}{\delta}\frac{a}{\lambda^2}=\frac{\epsilon\alpha^2}{\sigma} \quad (2.11)$$

so that the instability threshold is expected to be

$$\frac{\epsilon\alpha^2}{\sigma}=O(1), \quad (2.12)$$

with the auxiliary conditions that

$$\epsilon\alpha\sim\frac{\sigma}{\alpha}\ll 1. \quad (2.13)$$

We shall examine two cases which satisfy (2.12) and (2.13):

Case (i) $\alpha\ll 1, \quad \epsilon=O(1), \quad \sigma=O(\alpha^2),$

Case (ii) $\alpha=O(1), \quad \sigma=O(\epsilon)\ll 1.$

In Case (i), the oscillation amplitude is much smaller than the ripple wavelength; the instability is found locally either around the crests or around the troughs. The analysis, which is close to that of Hall for a cylinder, will only be sketched. In Case (ii), the oscillation amplitude is still smaller than the radius of curvature, but is comparable to the ripple wavelength. The disturbances at adjacent crests/troughs start to interact with each other. As a result the physical feature is now drastically different from that in Case (i) or in the case of a cylinder.

3. Two-dimensional basic flow

Before three-dimensional unstable disturbances are introduced, the basic flow is assumed to be two-dimensional in the plane of ξ and η with velocity components denoted by (U, V). It is convenient to introduce the stream function ψ defined by

$$U = \frac{1}{J^{\frac{1}{2}}}\frac{\partial \psi}{\partial \eta}, \quad V = -\frac{1}{J^{\frac{1}{2}}}\frac{\partial \psi}{\partial \xi}, \tag{3.1}$$

which automatically satisfies (2.4). Then the two-dimensional Navier–Stokes equations can be combined to give the vorticity equation

$$\frac{\partial}{\partial t}\nabla^2\psi - \alpha\frac{\partial(\psi, (1/J)\nabla^2\psi)}{\partial(\xi, \eta)} = \nabla^2\left(\frac{1}{J}\nabla^2\psi\right), \quad \eta > 0, \tag{3.2}$$

where

$$\nabla^2 \equiv \sigma^2\frac{\partial^2}{\partial \xi^2} + \frac{\partial^2}{\partial \eta^2} \tag{3.3}$$

is a distorted Laplacian. The boundary conditions are

$$\psi = \frac{\partial \psi}{\partial \eta} = 0, \quad \eta = 0, \tag{3.4a, b}$$

$$\frac{\partial \psi}{\partial \xi} = 0, \quad \frac{\partial \psi}{\partial \eta} = \cos t, \quad \eta \sim \infty. \tag{3.5a, b}$$

In addition, ψ is periodic in ξ with the period equal to unity.

Although the parameters are different, the method of perturbation can be used, as in Lyne (1971), to obtain the leading-order approximation, which is formally the same as the Stokes solution. In particular, for Case (i), $\sigma = O(\alpha^2) \ll 1$, we introduce a perturbation series in powers of α,

$$\psi = \psi_0 + \alpha\psi_1 + \ldots. \tag{3.6}$$

we expand similarly

$$J = \tilde{J} + O(\alpha^2), \tag{3.7}$$

where

$$\tilde{J} = 1 - 4\pi\epsilon\cos(2\pi\xi) + 4\pi^2\epsilon^2. \tag{3.8}$$

To the leading order, $O(\alpha^0)$, (3.2) and (3.4) give

$$\frac{\partial^2}{\partial \eta^2}\left[\frac{\partial \psi_0}{\partial t} - \frac{1}{\tilde{J}}\frac{\partial^2 \psi_0}{\partial \eta^2}\right] = 0, \tag{3.9}$$

$$\psi_0 = \frac{\partial \psi_0}{\partial \eta} = 0, \quad \eta = 0. \tag{3.10}$$

At infinity only (3.5b) can be satisfied:

$$\frac{\partial \psi_0}{\partial \eta} = \cos t, \quad \eta \sim \infty. \tag{3.11}$$

In this boundary-value problem the coordinate ξ is only a parameter. The solution is simply that of Stokes boundary layer over a plane:

$$\psi_0 = \tfrac{1}{2}e^{it}\left[\eta + \frac{1}{\tilde{\gamma}}(1 - e^{\tilde{\gamma}\eta})\right] + *, \tag{3.12}$$

where * denotes the complex-conjugate of the term preceding and

$$\tilde{\gamma} = \frac{-1-\mathrm{i}}{\sqrt{2}} \tilde{J}^{\frac{1}{2}}. \tag{3.13}$$

To this order, $O(\alpha^0)$, the corresponding velocity components are

$$U = \frac{1}{\tilde{J}^{\frac{1}{2}}} \frac{\partial \psi_0}{\partial \eta} + O(\alpha) = \frac{1}{2} \frac{1}{\tilde{J}^{\frac{1}{2}}} \mathrm{e}^{\mathrm{i}t}(1-\mathrm{e}^{\tilde{\gamma}\eta}) + * + O(\alpha), \tag{3.14}$$

$$V = -\frac{1}{\tilde{J}^{\frac{1}{2}}} \frac{\partial \psi_0}{\partial \xi} + O(\alpha) = -\epsilon \sin(2\pi\xi) \left\{ 2\pi^2 \frac{\tilde{\gamma}}{\tilde{J}^{\frac{3}{2}}} \mathrm{e}^{\mathrm{i}t} \left[-\frac{1}{\tilde{\gamma}^2}(1-\mathrm{e}^{\tilde{\gamma}\eta}) - \frac{\eta}{\tilde{\gamma}} \mathrm{e}^{\tilde{\gamma}\eta} \right] + * \right\} + O(\alpha). \tag{3.15}$$

Since for later analysis of instabilities we shall only consider leading approximations for $\alpha \ll 1$, (3.14) is sufficiently accurate, while (3.15) is never needed.

For Case (ii), $\alpha = O(1)$, $\epsilon = O(\sigma) \ll 1$, the ripple amplitude is comparable with the Stokes-layer thickness. The approximate solution can be sought in powers of ϵ. To the leading order, $O(\epsilon^0)$, we have

$$\tilde{J} = 1 + O(\epsilon), \quad \tilde{\gamma} = \gamma + O(\epsilon) = \frac{-1-\mathrm{i}}{\sqrt{2}} + O(\epsilon), \tag{3.16}$$

and the solution is simply that of Stokes in the curvilinear coordinates

$$U = \tfrac{1}{2} \mathrm{e}^{\mathrm{i}t}(1-\mathrm{e}^{\gamma\eta}) + * + O(\epsilon), \tag{3.17}$$

$$V = O(\epsilon). \tag{3.18}$$

This is so because the ripple slope is so small that convective inertia is negligible. A more detailed higher-order analysis of the two dimensional oscillatory flow over ripples can be found in Hara & Mei (1990). We recall that in the limit of a flat plate ($\epsilon = ka \to 0$), the Stokes solution is exact in principle for all α, though in reality it is limited by transition to turbulence at some experimentally observed threshold $Re = \sqrt{2}A/\delta = \sqrt{2\alpha/\sigma} \approx 500$. For small but finite ϵ the threshold of Re must be reduced, though it can be expected to be still large for small enough ϵ. Note also that when a cylinder of radius R oscillates in calm water, the Stokes boundary-layer flow is formed without separation around the cylinder at the leading order if $A/R \ll 1$. In our case, the local radius of curvature is $R \sim \lambda^2/a$ which is also much larger than the oscillation amplitude A since $A/R \sim \alpha\epsilon \ll 1$; we therefore expect the Stokes solution to hold at the leading order in ϵ as long as $\alpha\epsilon$ is sufficiently small.

4. Order estimates for three-dimensional disturbances

Let u', v', w' and p' be the three-dimensional disturbances superimposed on the two-dimensional basic flow found in §3. We substitute

$$u = U + u', \quad v = V + v', \quad w = w', \quad p = P + p' \tag{4.1}$$

into (2.4)–(2.7) with $u', v', w' \ll U, V$ and $p' \ll P$. After linearizing, the equations governing the disturbances read

$$\frac{\partial(J^{\frac{1}{2}}u')}{\partial \xi} + \frac{\partial(J^{\frac{1}{2}}v')}{\partial \eta} + J\frac{\partial w'}{\partial z} = 0, \tag{4.2}$$

$$\frac{\partial u'}{\partial t}+\alpha\left[U\frac{1}{J^{\frac{1}{2}}}\frac{\partial u'}{\partial \xi}+u'\frac{1}{J^{\frac{1}{2}}}\frac{\partial U}{\partial \xi}+V\frac{1}{J^{\frac{1}{2}}}\frac{\partial u'}{\partial \eta}+v'\frac{1}{J^{\frac{1}{2}}}\frac{\partial U}{\partial \eta}+\frac{Uv'}{J}\frac{\partial J^{\frac{1}{2}}}{\partial \eta}+\frac{u'V}{J}\frac{\partial J^{\frac{1}{2}}}{\partial \eta}\right]-\alpha\sigma^2\frac{2Vv'}{J}\frac{\partial J^{\frac{1}{2}}}{\partial \xi}$$

$$=-\frac{1}{J^{\frac{1}{2}}}\frac{\partial p'}{\partial \xi}-\sigma^2\frac{1}{J^{\frac{1}{2}}}\frac{\partial}{\partial \eta}\left[\frac{1}{J}\frac{\partial(J^{\frac{1}{2}}v')}{\partial \xi}\right]-\frac{1}{J^{\frac{1}{2}}}\frac{\partial}{\partial \eta}\left[-\frac{1}{J}\frac{\partial(J^{\frac{1}{2}}u')}{\partial \eta}\right]$$

$$+\frac{1}{J^{\frac{1}{2}}}\frac{\partial}{\partial z}\left[J^{\frac{1}{2}}\frac{\partial u'}{\partial z}\right]+\sigma^2\frac{1}{J^{\frac{1}{2}}}\frac{\partial}{\partial z}\left[-\frac{\partial w'}{\partial \xi}\right], \tag{4.3}$$

$$\frac{\partial v'}{\partial t}+\alpha\left[U\frac{1}{J^{\frac{1}{2}}}\frac{\partial v'}{\partial \xi}+u'\frac{1}{J^{\frac{1}{2}}}\frac{\partial V}{\partial \xi}+V\frac{1}{J^{\frac{1}{2}}}\frac{\partial v'}{\partial \eta}+v'\frac{1}{J^{\frac{1}{2}}}\frac{\partial V}{\partial \eta}+\frac{Uv'}{J}\frac{\partial J^{\frac{1}{2}}}{\partial \xi}+\frac{u'V}{J}\frac{\partial J^{\frac{1}{2}}}{\partial \xi}\right]-\alpha\frac{1}{\sigma^2}\frac{2Uu'}{J}\frac{\partial J^{\frac{1}{2}}}{\partial \eta}$$

$$=-\frac{1}{\sigma^2}\frac{1}{J^{\frac{1}{2}}}\frac{\partial p'}{\partial \eta}-\frac{1}{J^{\frac{1}{2}}}\frac{\partial}{\partial z}\left[\frac{\partial w'}{\partial \eta}-J^{\frac{1}{2}}\frac{\partial v'}{\partial z}\right]+\sigma^2\frac{1}{J^{\frac{1}{2}}}\frac{\partial}{\partial \xi}\left[\frac{1}{J}\frac{\partial(J^{\frac{1}{2}}v')}{\partial \xi}\right]-\frac{1}{J^{\frac{1}{2}}}\frac{\partial}{\partial \xi}\left[\frac{1}{J}\frac{\partial(J^{\frac{1}{2}}u')}{\partial \eta}\right], \tag{4.4}$$

$$\frac{\partial w'}{\partial t}+\alpha\left(U\frac{1}{J^{\frac{1}{2}}}\frac{\partial w'}{\partial \xi}+V\frac{1}{J^{\frac{1}{2}}}\frac{\partial w'}{\partial \eta}\right)$$

$$=-\frac{1}{\sigma^2}\frac{\partial p'}{\partial z}-\frac{1}{J^{\frac{1}{2}}}\frac{\partial}{\partial \xi}\left[J^{\frac{1}{2}}\frac{\partial u'}{\partial z}\right]-\sigma^2\frac{1}{J}\frac{\partial}{\partial \xi}\left(-\frac{\partial w'}{\partial \xi}\right)+\frac{1}{J}\frac{\partial}{\partial \eta}\left(\frac{\partial w'}{\partial \eta}-J^{\frac{1}{2}}\frac{\partial v'}{\partial z}\right). \tag{4.5}$$

Consider first the vertical momentum (4.4). The leading inertia term is v'_t which is of the same order as the leading viscous stress terms on the right. On the left the centrifugal force (the last term) can be of comparable importance if

$$v'_t\sim\frac{\alpha}{\sigma^2}Uu'\frac{\partial J^{\frac{1}{2}}}{\partial \eta}\sim\frac{\epsilon\alpha}{\sigma}u' \tag{4.6}$$

upon using (2.8), hence

$$O(v')=O\left(\frac{\epsilon\alpha}{\sigma}u'\right). \tag{4.7}$$

Now consider the tangential momentum (4.3). Among the convective inertia terms the largest is the fourth

$$\frac{\alpha v'}{J^{\frac{1}{2}}}\frac{\partial U}{\partial \eta}, \tag{4.8}$$

which is of the order

$$O\left(\frac{\epsilon\alpha^2}{\sigma}u'\frac{1}{J^{\frac{1}{2}}}\frac{\partial U}{\partial \eta}\right)=O\left(\frac{\epsilon\alpha^2}{\sigma}u'\right) \tag{4.9}$$

when (4.7) is satisfied. Therefore the centrifugal force plays an important role in both momentum equations of the disturbance if

$$\frac{\epsilon\alpha^2}{\sigma}=O(1) \tag{4.10}$$

as has been found by Hall. It follows from (4.7) that

$$O(u')=O(\alpha v'). \tag{4.11}$$

From the continuity we must have $w'=O(v')$. Thus for Case (i), $u'=O(\alpha v')\ll v'$ and $w'=O(v')$ while for Case (ii), $u'\sim v'\sim w'$. In (4.4) and (4.5), the pressure gradient is balanced with inertia and viscous terms by setting $p'=O(\sigma^2 v')\sim O(\sigma^2 w')$ in both cases.

We now study the two cases separately.

5. Case (i). Weak ambient oscillations and finite ripple slope: $\alpha \ll 1$, $\sigma = O(\alpha^2) \ll 1$, $\epsilon = O(1)$. Linearized equations for three-dimensional disturbances

In view of (4.11), we now rescale u', v', w' and p' by changing them as follows:

$$u' \to \alpha u', \quad v' \to v', \quad w' \to w', \quad p' \to \sigma^2 p' \tag{5.1}$$

and keep only the $O(\alpha^0)$ terms in the linearized equations.

It is now convenient to introduce the final transformation:

$$\left.\begin{aligned} \hat{U} = \tilde{J}^{\frac{1}{2}} U, \quad \hat{u} = \tilde{J}^{\frac{1}{2}} u', \quad \hat{v} = v', \quad \hat{w} = w', \quad \hat{p} = p' \\ \hat{\xi} = \xi, \quad \hat{\eta} = \tilde{J}^{\frac{1}{2}} \eta, \quad \hat{z} = z, \quad \hat{t} = t. \end{aligned}\right\} \tag{5.2}$$

Note that the derivatives are transformed according to

$$\frac{\partial}{\partial \eta} \to \tilde{J}^{\frac{1}{2}} \frac{\partial}{\partial \hat{\eta}}, \quad \frac{\partial}{\partial z} \to \frac{\partial}{\partial \hat{z}}, \quad \frac{\partial}{\partial t} \to \frac{\partial}{\partial \hat{t}}. \tag{5.3}$$

The linearized equations (4.2)–(4.5) for the disturbance become

$$\frac{\partial \hat{v}}{\partial \hat{\eta}} + \frac{\partial \hat{w}}{\partial \hat{z}} = 0, \tag{5.4}$$

$$\frac{\partial \hat{u}}{\partial \hat{t}} - \frac{\partial^2 \hat{u}}{\partial \hat{z}^2} - \frac{\partial^2 \hat{u}}{\partial \hat{\eta}^2} + \frac{\partial \hat{U}}{\partial \hat{\eta}} \hat{v} = 0, \tag{5.5}$$

$$\frac{\partial \hat{v}}{\partial \hat{t}} - \frac{\partial^2 \hat{v}}{\partial \hat{z}^2} + \frac{\partial \hat{p}}{\partial \hat{\eta}} + \frac{\partial^2 \hat{w}}{\partial \hat{\eta}\, \partial \hat{z}} - 8\pi^2 \hat{U} \hat{u} T_{\mathrm{L}} = 0, \tag{5.6}$$

$$\frac{\partial \hat{w}}{\partial \hat{t}} - \frac{\partial^2 \hat{w}}{\partial \hat{\eta}^2} + \frac{\partial \hat{p}}{\partial \hat{z}} + \frac{\partial^2 \hat{v}}{\partial \hat{\eta}\, \partial \hat{z}} = 0, \tag{5.7}$$

where

$$T_{\mathrm{L}} = \frac{T[\cos(2\pi\hat{\xi}) - 2\pi\epsilon]}{\tilde{J}^{\frac{5}{2}}} = \frac{\epsilon\alpha^2}{\sigma} \frac{[\cos(2\pi\hat{\xi}) - 2\pi\epsilon]}{[1 - 4\pi\epsilon\cos(2\pi\hat{\xi}) + 4\pi^2\epsilon^2]^{\frac{5}{2}}}. \tag{5.8}$$

The boundary conditions are

$$\hat{u} = \hat{v} = \hat{w} = \hat{p} = 0, \quad \hat{\eta} = 0, \infty. \tag{5.9}$$

The basic tangential flow (3.14) is now simply

$$\hat{U} = \tfrac{1}{2} e^{it}(1 - e^{\gamma\hat{\eta}}) + *, \quad \gamma = \frac{-1-i}{\sqrt{2}}. \tag{5.10}$$

Equations (5.4)–(5.9) constitute a homogeneous boundary-value problem similar to that studied by Hall for a circular cylinder.

Note from (3.14) that the local oscillation amplitude just outside the Stokes boundary layer is

$$A_{\mathrm{L}} = A\tilde{J}^{-\frac{1}{2}} \tag{5.11}$$

and that the local radius of curvature of the ripple at $\hat{\xi}$ is

$$R_{\mathrm{L}} = \frac{1}{4\pi^2} \frac{\lambda^2}{a} \frac{\tilde{J}^{\frac{3}{2}}}{[\cos(2\pi\hat{\xi}) - 2\pi\epsilon]} \tag{5.12}$$

(see Appendix A). Hence

$$T_{\mathrm{L}} = \frac{1}{4\pi^2} \frac{A_{\mathrm{L}}^2}{\delta R_{\mathrm{L}}} \tag{5.13}$$

is the local Taylor number. At the leading order in α the linearized disturbance depends on $\hat{\xi}$ only parametrically through T_L. It is only this detail that is different from the circular cylinder case of Hall.

The remaining analysis is carried out as in Hall by first eliminating $\hat{w}$ and $\hat{p}$ after cross-differentiation. We then specify the dependence along the ripple to be sinusoidal in z with wavenumber k. Because the coefficients depend on time sinusoidally through $\hat{U}$ we consider the solution of the form:

$$\begin{pmatrix} \hat{u} \\ \hat{v} \end{pmatrix} = \cos k\hat{z}\, e^{s\hat{t}} \sum_{n=-\infty}^{\infty} \begin{pmatrix} u_n(\hat{\eta}) \\ v_n(\hat{\eta}) \end{pmatrix} e^{in\hat{t}}, \tag{5.14}$$

where s corresponds to the rate of growth, or decay. The corresponding expression for $\hat{w}$ is similar except $\cos k\hat{z}$ is replaced by $\sin k\hat{z}$. The result is an eigenvalue problem for a linear system of coupled ordinary differential equations in $\hat{\eta}$. For neutral instability ($s = 0$) or prescribed rate of growth we fix the wavenumber k and solve for the eigenfunctions and the eigenvalue T_L. The computational procedure is essentially that of Hall. Since its extension is described in Appendix B for Case (ii) it is omitted here.

Although we originally assumed that the ripple slope is finite ($\epsilon = O(1)$), the present theory should be valid in the limit of $\epsilon \ll 1$ as long as the Taylor number remains of $O(1)$. This means that the results from the small-ϵ limit of this theory for small α should agree with the small-α limit of the theory for small ϵ. This will be confirmed later.

6. Case (i). Results and discussion

The controlling parameter of the problem is the local Taylor number, defined by (5.8) which is a function of $\hat{\xi}$, ϵ and α^2/σ. For fixed α^2/σ, the typical dependence of T_L on the location $\hat{\xi}$ and the ripple slope ϵ is plotted in figure 2. When $\epsilon \leqslant 1/8\pi \approx 0.040$, T_L varies monotonically between the positive extremum

$$T_L(\hat{\xi} = 0) = \frac{\alpha^2}{\sigma} \frac{\epsilon}{(1-2\pi\epsilon)^4} \tag{6.1}$$

at the crest, to the negative extremum

$$T_L(\hat{\xi} = 0.5) = -\frac{\alpha^2}{\sigma} \frac{\epsilon}{(1+2\pi\epsilon)^4} \tag{6.2}$$

at the trough. For $\epsilon \geqslant 1/8\pi$ the negative extremum occurs somewhere between the trough and the crest. As will be shown shortly, the absolute value of the local Taylor number must exceed a certain threshold before instability becomes possible at any wavenumber. Thus instability must commence at the location where T_L is either the positive maximum or the negative minimum. This is the main distinction from the case of a circular cylinder studied by Hall, where T_L is always positive. In figure 3 we plot the relation between T_L (both positive and negative) and k for various growth rates s. The curves for $s = 0$ correspond to neutral instability and are concave away from the k-axis. Curves with positive growth rates are inside the neutral instability curves. In particular, the smallest positive threshold is at $T_L = 0.430$ and $k = 0.36$ and the numerically smallest negative threshold is $T_L = -0.255$ and $k = 0.31$. The positive threshold is identical to that obtained by Hall (1984) for a circular cylinder. Since, for sufficiently large ϵ, the absolute value of the positive maximum of T_L is

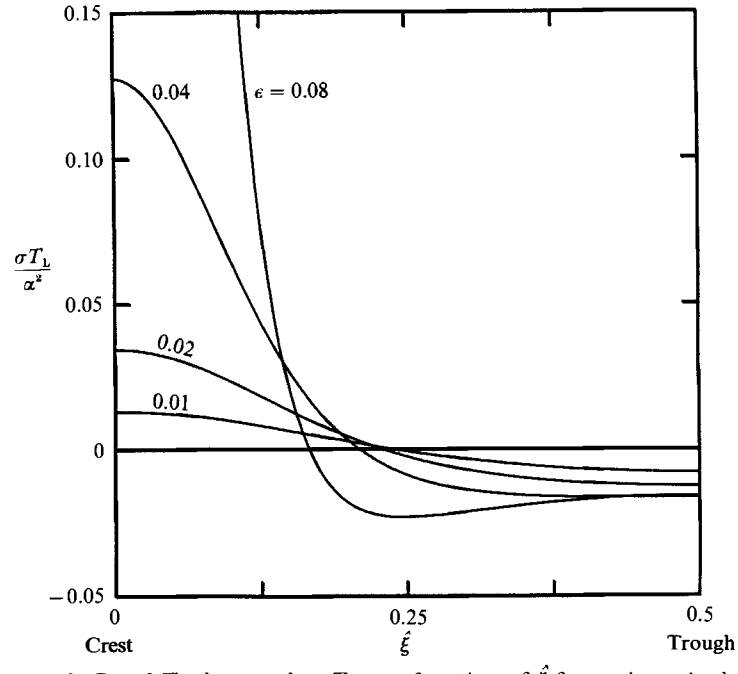

FIGURE 2. Local Taylor number T_L as a function of $\hat{\xi}$ for various ripple slopes ϵ.

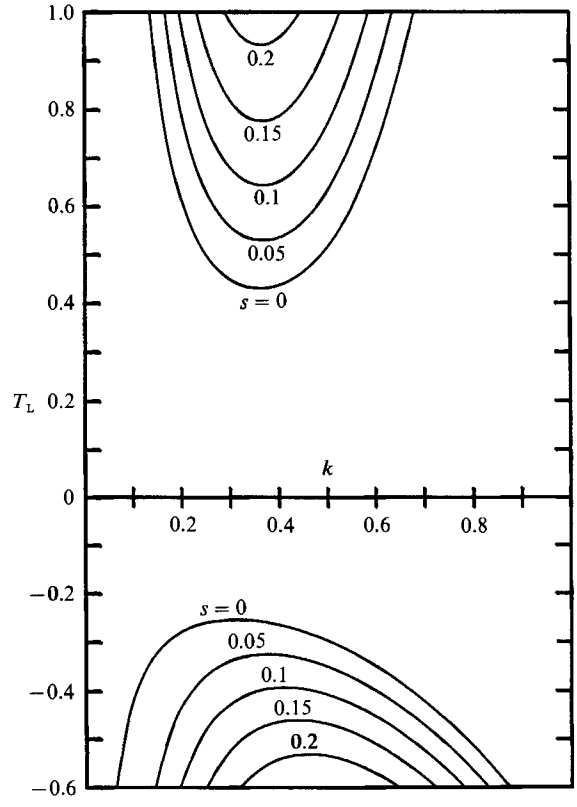

FIGURE 3. Relationship between local Taylor number T_L and disturbance wavelength k for various growth rates s.

much larger than that of the negative minimum (cf. figure 2); instability should occur first at the crest as α^2/σ increases. This is of course because the crest has a sharper curvature than the trough for all but very small ϵ. On the other hand, for very small ϵ the curvatures at the crests and the troughs become equal. Instability can occur at the trough first before the crest. The demarcation value of ϵ for the same α^2/σ is found by equating α^2/σ in (6.1) and (6.2),

$$\frac{\alpha^2}{\sigma} = \frac{(1-2\pi\epsilon)^4}{\epsilon} \times 0.430 = \frac{(1+2\pi\epsilon)^4}{\epsilon} \times 0.255, \tag{6.3}$$

i.e. $\epsilon = 0.0103$ and $\alpha^2/\sigma = 31.7$. Thus for $\epsilon < 0.0103$ instability first ocurs at the trough when α^2/σ increases past 31.7. For $\epsilon > 0.0103$, instability always occurs at the crest first. In the limit of $\epsilon \to 0$, the threshold of instability becomes simply

$$T = \frac{\epsilon\alpha^2}{\sigma} = 0.255 \tag{6.4}$$

for the trough mode, and

$$T = \frac{\epsilon\alpha^2}{\sigma} = 0.430 \tag{6.5}$$

for the crest mode.

As in the instability along a circular cylinder studied by Hall, the disturbance is localized in a small region around the crests or the troughs, whose width in $\hat{\xi}$-direction is of $O(\alpha^{\frac{1}{2}})$. The $\hat{\xi}$-dependence of this unstable mode may be obtained from the higher-order perturbation equations in α. Since the results do not give any new features and the nonlinear analysis is very similar to Hall's, they are not presented here. Readers may refer to Hara (1990) for further information.

7. Case (ii). Moderately strong ambient oscillations and gentle ripples: $\alpha = O(1)$, $\sigma = O(\epsilon) \ll 1$. Equations for three-dimensional disturbances

For small ϵ and $\sigma = O(\epsilon)$, the ripple amplitude is comparable with the Stokes-layer thickness. It is still necessary to employ the curvilinear coordinates ξ and η. As shown in (3.16)–(3.18), the Jacobian of transformation is now approximately unity and the basic two-dimensional flow is formally that of a Stokes boundary layer over a flat plate in the (ξ, η)-plane.

In the linearized equations (4.2)–(4.5), we now set $\epsilon = O(\sigma)$ and $\epsilon\alpha^2/\sigma = O(1)$ and rescale the pressure by changing p' to $\sigma^2 p'$. To the leading order, $O(\epsilon^0)$, the approximate equations are

$$\frac{\partial u'}{\partial \xi} + \frac{\partial v'}{\partial \eta} + \frac{\partial w'}{\partial z} = 0, \tag{7.1}$$

$$\frac{\partial u'}{\partial t} - \frac{\partial^2 u'}{\partial \eta^2} - \frac{\partial^2 u'}{\partial z^2} + U\alpha\frac{\partial u'}{\partial \xi} + \frac{\partial U}{\partial \eta}\alpha v' = 0, \tag{7.2}$$

$$\frac{\partial v'}{\partial t} + \frac{\partial^2 w'}{\partial \eta\,\partial z} - \frac{\partial^2 v'}{\partial z^2} + \frac{\partial^2 u'}{\partial \xi\,\partial \eta} + U\alpha\frac{\partial v'}{\partial \xi} - 8\pi^2 U\cos(2\pi\xi)\frac{T}{\alpha}u' + \frac{\partial p'}{\partial \eta} = 0, \tag{7.3}$$

$$\frac{\partial w'}{\partial t} - \frac{\partial^2 w'}{\partial \eta^2} + \frac{\partial^2 v'}{\partial \eta\,\partial z} + \frac{\partial^2 u'}{\partial \xi\,\partial z} + U\alpha\frac{\partial w'}{\partial \xi} + \frac{\partial p'}{\partial z} = 0, \tag{7.4}$$

with the boundary conditions

$$u' = v' = w' = 0, \quad \eta = 0, \infty. \tag{7.5}$$

After eliminating w' and p' by cross-differentiation, we seek disturbances which are sinusoidal in z,

$$u' = \hat{u}\cos kz, \quad v' = \hat{v}\cos kz, \tag{7.6}$$

where k is the wavenumber along the ripple. The corresponding form for w' is $w' = \hat{w}\sin kz$. Let us further introduce a coordinate system oscillating with the ambient fluid:

$$\tilde{\xi} = \xi - \alpha\sin t \tag{7.7}$$

so that

$$\frac{\partial}{\partial t} \to \frac{\partial}{\partial t} - \alpha\cos t\frac{\partial}{\partial\tilde{\xi}}, \quad \frac{\partial}{\partial\xi} \to \frac{\partial}{\partial\tilde{\xi}}. \tag{7.8}$$

The coordinates η and z remain unchanged. The governing equations for $\hat{u}$ and $\hat{v}$ are then found to be

$$\left(\frac{\partial^2}{\partial\eta^2} - k^2 - \frac{\partial}{\partial t}\right)\left(\frac{\partial^2}{\partial\eta^2} - \kappa^2\right)\hat{v} - (U - \cos t)\,\alpha\left(\frac{\partial^2}{\partial\eta} - k^2\right)\frac{\partial\hat{v}}{\partial\tilde{\xi}} + \frac{\partial^2 U}{\partial\eta^2}\alpha\frac{\partial\hat{v}}{\partial\tilde{\xi}} - 8\pi^2 U\cos\left[2\pi(\tilde{\xi} + \alpha\sin t)\right]\frac{T}{\alpha}k^2\hat{u} = 0, \tag{7.9}$$

$$\left(\frac{\partial^2}{\partial\eta^2} - k^2 - \frac{\partial}{\partial t}\right)\hat{u} - (U - \cos t)\,\alpha\frac{\partial\hat{u}}{\partial\tilde{\xi}} - \frac{\partial U}{\partial\eta}\alpha\hat{v} = 0, \tag{7.10}$$

with the boundary conditions

$$\hat{u} = \hat{v} = \frac{\partial\hat{v}}{\partial\eta} = 0, \quad \eta = 0, \infty, \tag{7.11}$$

where, in view of (3.17),

$$U - \cos t = -\tfrac{1}{2}\mathrm{e}^{\mathrm{i}t}\mathrm{e}^{\gamma\eta} + *, \quad \frac{\partial U}{\partial\eta} = -\tfrac{1}{2}\gamma\,\mathrm{e}^{\mathrm{i}t}\mathrm{e}^{\gamma\eta} + *, \quad \frac{\partial^2 U}{\partial\eta^2} = -\tfrac{1}{2}\mathrm{i}\,\mathrm{e}^{\mathrm{i}t}\mathrm{e}^{\gamma\eta} + *. \tag{7.12}$$

With the transformation (7.7) the coefficient $U(\eta) - \cos t$ vanishes at $\eta \sim \infty$ along with $\partial U/\partial\eta$ and $\partial^2 U/\partial\eta^2$. The asymptotic equations for the time harmonics of $\hat{u}$ are uncoupled and can be solved analytically as shown in Appendix B. The variable coefficient appearing in (7.9) can be expanded using the well-known identities (Abramowitz & Stegun 1965, p. 361):

$$\cos(2\pi\alpha\sin t) = \sum_{n=\pm\text{even}} \mathrm{e}^{\mathrm{i}nt} J_n(2\pi\alpha), \tag{7.13}$$

$$\sin(2\pi\alpha\sin t) = \sum_{n=\pm\text{odd}} \frac{\mathrm{e}^{\mathrm{i}nt}}{\mathrm{i}} J_n(2\pi\alpha), \tag{7.14}$$

so that

$$\begin{aligned}\cos\left[2\pi(\tilde{\xi} + \alpha\sin t)\right] &= \cos(2\pi\tilde{\xi})\cos(2\pi\alpha\sin t) - \sin(2\pi\tilde{\xi})\sin(2\pi\alpha\sin t)\\ &= \tfrac{1}{2}(\mathrm{e}^{\mathrm{i}2\pi\tilde{\xi}} + \mathrm{e}^{-\mathrm{i}2\pi\tilde{\xi}}) \sum_{n=\pm\text{even}} \mathrm{e}^{\mathrm{i}nt} J_n(2\pi\alpha)\\ &\quad - \frac{\mathrm{e}^{\mathrm{i}2\pi\tilde{\xi}} - \mathrm{e}^{-\mathrm{i}2\pi\tilde{\xi}}}{2\mathrm{i}} \sum_{n=\pm\text{odd}} \frac{\mathrm{e}^{\mathrm{i}nt}}{\mathrm{i}} J_n(2\pi\alpha)\\ &= \sum_{n=-\infty}^{\infty} \mathrm{e}^{\mathrm{i}nt} J_n(2\pi\alpha)\,\tfrac{1}{2}(\mathrm{e}^{\mathrm{i}2\pi\tilde{\xi}} + (-1)^n\,\mathrm{e}^{-\mathrm{i}2\pi\tilde{\xi}}).\end{aligned} \tag{7.15}$$

We now seek the solution in the following form:

$$\begin{pmatrix}\hat{u}\\ \hat{v}\end{pmatrix} = \sum_{n=-\infty}^{\infty}\sum_{m=-\infty}^{\infty}\begin{pmatrix}u_{nm}(\eta)\\ v_{nm}(\eta)\end{pmatrix} e^{int}\, e^{im\pi\tilde{\xi}}\, e^{st}, \tag{7.16}$$

where s is real, and represents the rate of growth or decay. After $\hat{u}$ and $\hat{v}$ are calculated, $i\hat{w}$ can be readily calculated by using (7.1). For reality of the solution we require that

$$u^*_{nm} = u_{-n,-m}, \quad v^*_{nm} = v_{-n,-m}. \tag{7.17}$$

Since the ripple period is unity, an even m corresponds to harmonic disturbance while an odd m corresponds to subharmonic disturbances. Also, in contrast to Case (i) for small α, the leading-order solution here depends explicitly on $\tilde{\xi}$. Substituing (7.16) into (7.9) and sorting out the harmonics we obtain for the coefficient of the typical term $\exp i(nt+m\pi\tilde{\xi})$:

$$\begin{aligned}&\left(\frac{\partial^2}{\partial\eta^2}-k^2-in-s\right)\left(\frac{\partial^2}{\partial\eta^2}-k^2\right)v_{nm}+\tfrac{1}{2}e^{\gamma\eta}\alpha im\pi\left(\frac{\partial^2}{\partial\eta^2}-k^2\right)v_{n-1,m}\\ &+\tfrac{1}{2}e^{\gamma^*\eta}\alpha im\pi\left(\frac{\partial^2}{\partial\eta^2}-k^2\right)v_{n+1,m}+\tfrac{1}{2}e^{\gamma\eta}\alpha m\pi v_{n-1,m}-\tfrac{1}{2}e^{\gamma^*\eta}\alpha m\pi v_{n+1,m}\\ &-2\pi^2k^2\frac{T}{\alpha}\sum_j\left[(1-e^{\gamma\eta})J_{j-1}(2\pi\alpha)+(1-e^{\gamma^*\eta})J_{j+1}(2\pi\alpha)\right]\left[u_{n-j,m-2}-(-1)^j u_{n-j,m+2}\right]=0.\end{aligned} \tag{7.18}$$

Similarly, substituting (7.16) into (7.10) and sorting out the harmonics give

$$\begin{aligned}&\left(\frac{\partial^2}{\partial\eta^2}-k^2-in-s\right)u_{nm}+\tfrac{1}{2}e^{\gamma\eta}\alpha im\pi u_{n-1,m}+\tfrac{1}{2}e^{\gamma^*\eta}\alpha im\pi u_{n+1,m}\\ &+\tfrac{1}{2}\gamma\, e^{\gamma\eta}\alpha v_{n-1,m}+\tfrac{1}{2}\gamma^* e^{\gamma^*\eta}\alpha v_{n+1,m}=0.\end{aligned} \tag{7.19}$$

The homogeneous boundary conditions for each harmonic are

$$u_{nm} = v_{nm} = \frac{\partial v_{nm}}{\partial\eta} = 0, \quad \eta = 0, \infty. \tag{7.20}$$

Equations (7.18) and (7.19) form an infinite set of coupled ordinary differential equations for u_{nm} and v_{nm}.

The numerical solution of this eigenvalue problem can be facilitated by noting first that the mth harmonic is coupled only with the $(m+2)$th and $(m-2)$th harmonics. Therefore we can consider the following two cases separately: m = even(harmonic) only and m = odd(subharmonic) only.

Let us take the complex-conjugate of (7.19):

$$\begin{aligned}&\left(\frac{\partial^2}{\partial\eta^2}-k^2+in-s\right)u^*_{nm}-\tfrac{1}{2}e^{\gamma^*\eta}\alpha im\pi u^*_{n-1,m}-\tfrac{1}{2}e^{\gamma\eta}\alpha im\pi u^*_{n+1,m}\\ &+\tfrac{1}{2}\gamma^* e^{\gamma^*\eta}\alpha v^*_{n-1,m}+\tfrac{1}{2}\gamma\, e^{\gamma\eta}\alpha v^*_{n+1,m}=0,\end{aligned} \tag{7.21}$$

and next replace n by $-n$ in (7.19):

$$\begin{aligned}&\left(\frac{\partial^2}{\partial\eta^2}-k^2+in-s\right)u_{-n,m}+\tfrac{1}{2}e^{\gamma\eta}\alpha im\pi u_{-n-1,m}+\tfrac{1}{2}e^{\gamma^*\eta}\alpha im\pi u_{-n+1,m}\\ &+\tfrac{1}{2}\gamma\, e^{\gamma\eta}\alpha v_{-n-1,m}+\tfrac{1}{2}\gamma^* e^{\gamma^*\eta}\alpha v_{-n+1,m}=0.\end{aligned} \tag{7.22}$$

These two equations are of course identical except for the change of indices; this leads to certain parity properties. Now if

$$u^*_{nm} = u_{-n,m} \tag{7.23a}$$

then the identity of (7.21) and (7.22) implies

$$-u^*_{n-1,m} = u_{-n+1,m}, \quad -u^*_{n+1,m} = u_{-n-1,m}, \tag{7.23b, c}$$

$$v^*_{n-1,m} = v_{-n+1,m}, \quad v^*_{n+1,m} = v_{-n-1,m}. \tag{7.23d, e}$$

On the other hand, if

$$-u^*_{nm} = u_{-n,m} \tag{7.24a}$$

then

$$u^*_{n-1,m} = u_{-n+1,m}, \quad u^*_{n+1,m} = u_{-n-1,m}, \tag{7.24b, c}$$

$$-v^*_{n-1,m} = v_{-n+1,m}, \quad -v^*_{n+1,m} = v_{-n-1,m}. \tag{7.24d, e}$$

When n = even, $n \pm 1$ = odd, (7.23a–e) can be expressed in a more compact form:

$$u^*_{nm} = (-1)^n u_{-n,m}, \quad v^*_{nm} = (-1)^{n+1} v_{-n,m}, \tag{7.25}$$

while (7.24a–e) can be expressed as

$$u^*_{nm} = (-1)^{n+1} u_{-n,m}, \quad v^*_{nm} = (-1)^n v_{-n,m}. \tag{7.26}$$

On the other hand, when n = odd, $n \pm 1$ = even, (7.23) is equivalent to (7.26) while (7.24) is equivalent to (7.25). Therefore for either n = even or odd, (7.25) and (7.26) are two possibilities. The same conclusion can be reached from (7.18) by similar arguments.

In summary, we expect four distinct types of disturbances:
Type I (subharmonic): m = odd, with (7.26),
Type II (subharmonic): m = odd, with (7.25),
Type III (harmonic): m = even, with (7.26),
Type IV (harmonic): m = even, with (7.25).

Let us examine the implications on the velocity components expressed by (7.17). For Type I we invoke (7.17) and (7.26) so that

$$\begin{aligned} \hat{u} &= \left\{ \sum_{n=-\infty}^{\infty} e^{int} \sum_{m=+\text{odd}} (e^{im\pi\tilde{\xi}} u_{nm} + e^{-im\pi\tilde{\xi}} u_{n,-m}) \right\} e^{st} \\ &= \left\{ \sum_{n=-\infty}^{\infty} e^{int} \sum_{m=+\text{odd}} [e^{im\pi\tilde{\xi}} u_{nm} + e^{-im\pi\tilde{\xi}} (-1)^{n+1} u_{nm}] \right\} e^{st} \end{aligned} \tag{7.27}$$

Since $[\cdot] = 2u_{nm} \cos(m\pi\tilde{\xi})$ for n = odd

and $[\cdot] = 2iu_{nm} \sin(m\pi\tilde{\xi})$ for n = even

we have

$$\hat{u} = \left[\sum_{n=\pm\text{odd}} e^{int} \sum_{m=+\text{odd}} 2\cos(m\pi\tilde{\xi})\, u_{nm} + \sum_{n=\pm\text{even}} e^{int} \sum_{m=+\text{odd}} 2i \sin(m\pi\tilde{\xi})\, u_{nm} \right] e^{st}. \tag{7.28}$$

Similarly,

$$\hat{v} = \left[\sum_{n=\pm\text{even}} e^{int} \sum_{m=+\text{odd}} 2\cos(m\pi\tilde{\xi})\, v_{nm} + \sum_{n=\pm\text{odd}} e^{int} \sum_{m=+\text{odd}} 2i \sin(m\pi\tilde{\xi})\, v_{nm} \right] e^{st} \tag{7.29}$$

for Type I. It is different from $\hat{u}$ in the range of the first summation.

By similar reasoning, the velocity components for the other three types have the following forms

Type II:

$$\hat{u} = \left[\sum_{n=\pm\text{even}} e^{int} \sum_{m=+\text{odd}} 2\cos(m\pi\tilde{\xi})\, u_{nm} + \sum_{n=\pm\text{odd}} e^{int} \sum_{m=+\text{odd}} 2i\sin(m\pi\tilde{\xi})\, u_{nm} \right] e^{st}, \tag{7.30}$$

$$\hat{v} = \left[\sum_{n=\pm\text{odd}} e^{int} \sum_{m=+\text{odd}} 2\cos(m\pi\tilde{\xi})\, v_{nm} + \sum_{n=\pm\text{even}} e^{int} \sum_{m=+\text{odd}} 2i\sin(m\pi\tilde{\xi})\, v_{nm} \right] e^{st}. \tag{7.31}$$

Thus $\hat{u}$ of Type II has the form of $\hat{v}$ of Type I and vice versa.

Type III:

$$\hat{u} = \left[\sum_{n=\pm\text{odd}} e^{int} \sum_{m=0,1,2,\ldots} 2\cos(2m\pi\tilde{\xi})\, u_{nm} + \sum_{n=\pm\text{even}} e^{int} \sum_{m=0,1,2,\ldots} 2i\sin(2m\pi\tilde{\xi})\, u_{nm} \right] e^{st}, \tag{7.32}$$

$$\hat{v} = \left[\sum_{n=\pm\text{even}} e^{int} \sum_{m=0,1,2,\ldots} 2\cos(2m\pi\tilde{\xi})\, v_{nm} + \sum_{n=\pm\text{odd}} e^{int} \sum_{m=0,1,2,\ldots} 2i\sin(2m\pi\tilde{\xi})\, v_{nm} \right] e^{st}. \tag{7.33}$$

Type IV:

$$\hat{u} = \left[\sum_{n=\pm\text{even}} e^{int} \sum_{m=0,1,2,\ldots} 2\cos(2m\pi\tilde{\xi})\, u_{nm} + \sum_{n=\pm\text{odd}} e^{int} \sum_{m=0,1,2,\ldots} 2i\sin(2m\pi\tilde{\xi})\, u_{nm} \right] e^{st}, \tag{7.34}$$

$$\hat{v} = \left[\sum_{n=\pm\text{odd}} e^{int} \sum_{m=0,1,2,\ldots} 2\cos(2m\pi\tilde{\xi})\, v_{nm} + \sum_{n=\pm\text{even}} e^{int} \sum_{m=0,1,2,\ldots} 2i\sin(2m\pi\tilde{\xi})\, v_{nm} \right] e^{st}. \tag{7.35}$$

Thus $\hat{u}$ of Type IV has the same form as $\hat{v}$ of Type III and vice versa.

For neutral instability, $s = 0$, the eigenfunctions $u_{nm}(\eta)$ and $v_{nm}(\eta)$ and the eigenvalue T must be solved from the boundary-value problem for given k. The numerical procedure is described in Appendix B, and computations were performed on a Cray X-MP super computer. For a prescribed growth rate $s > 0$, the eigenvalue T is solved similarly for given k. In the following section only the neutral instability will be discussed. The modal analysis of the form (7.16) suggests that the instability now spans over the entire ripple surface. Hence the eigenvalue T is of global significance in contrast to the local Taylor number T_L in Case (i).

8. Case (ii). Neutral instability curves and mean flow patterns

In figures 4(*a*) to 4(*d*) we plot for $\alpha = 1/2\pi, 1/\pi, 3/2\pi, 2/\pi \approx 0.16, 0.32, 0.48, 0.64$ the neutral instability curves of T *vs.* k. For each of the four types of disturbances, the number of curves increases with the Taylor number T, corresponding to the proliferation of modes. For identification we assign the modal number in the order of increasing threshold Taylor number. In some cases two different types share essentially the same neutral curve. Since they have different flow structures, two modal numbers are assigned. The qualitative features of the results for non-zero growth rates are similar to those in Case (i), and are not presented here.

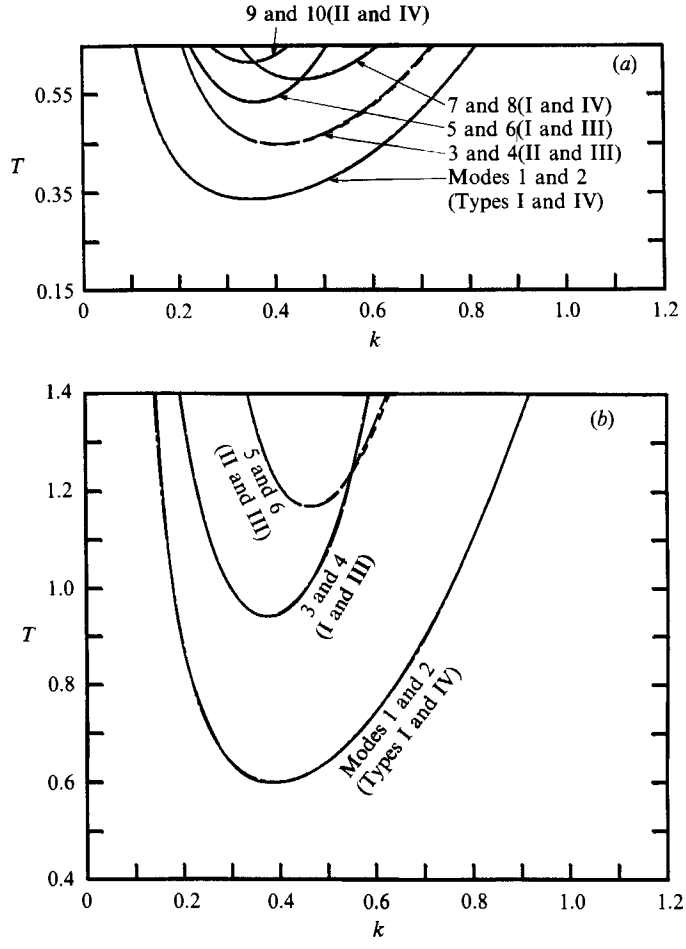

FIGURE 4(*a*, *b*). For caption see facing page.

Each mode is distinguished by its flow pattern which is in general periodic in time. For simplicity, we choose to examine each mode by its time-averaged tangential velocity vectors near the ripple surface (small $\eta > 0$). These time averages correspond physically to the Eulerian induced streaming which should be responsible for the drifting of small particles near the ripple surface, and are obtained by first transforming from the oscillating to the stationary (ξ, η, z)-coordinates. For example, for Type I we first calculate u' by expanding (7.28) with the help of (7.15):

$$u' = \cos kz \Bigg\{ \sum_{n=\pm\text{odd}} e^{int} \sum_{m=+\text{odd}} 2\cos[m\pi(\xi - \alpha \sin t)]\, u_{nm} + \sum_{n=\pm\text{even}} e^{int} \sum_{m=+\text{odd}} 2i \sin[m\pi(\xi - \alpha \sin t)]\, u_{nm} \Bigg\}$$

$$= \cos kz \Bigg\{ \sum_{n=\pm\text{odd}} e^{int} \sum_{m=+\text{odd}} \sum_{j=-\infty}^{\infty} e^{-ijt} J_j(m\pi\alpha) [e^{im\pi\xi} + (-1)^j e^{-im\pi\xi}]\, u_{nm} + \sum_{n=\pm\text{even}} e^{int} \sum_{m=+\text{odd}} \sum_{j=-\infty}^{\infty} e^{-ijt} J_j(m\pi\alpha) [e^{im\pi\xi} - (-1)^j e^{-im\pi\xi}]\, u_{nm} \Bigg\}$$

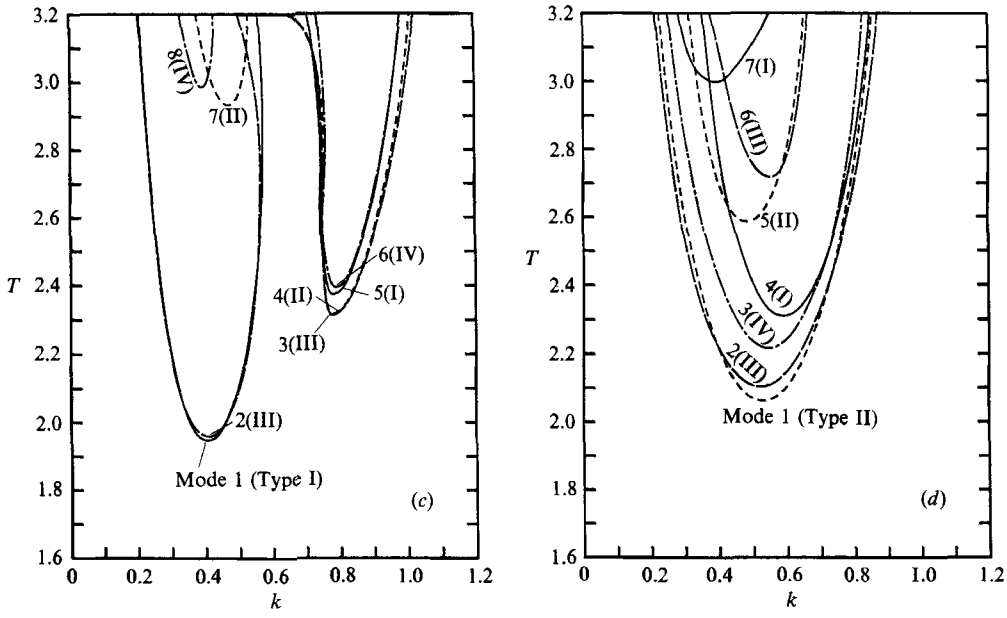

FIGURE 4. Relationship between Taylor number T and disturbance wavelength k for neutral instability ($s = 0$). ——, Type I; - - - - -, Type II; — —, Type III; — — —, Type IV. (*a*) $\alpha = 1/2\pi \approx 0.16$, (*b*) $\alpha = 1/\pi \approx 0.32$, (*c*) $\alpha = 3/2\pi \approx 0.48$, (*d*) $\alpha = 2/\pi \approx 0.64$.

$$= \cos kz \Bigg[\sum_{n=\pm\text{odd}} e^{int} \sum_{m=+\text{odd}} 2\cos(m\pi\xi) \sum_{j=-\infty}^{\infty} J_j(m\pi\alpha)\, u_{n+j,m} + \sum_{n=\pm\text{even}} e^{int} \sum_{m=+\text{odd}} 2i\sin(m\pi\xi) \sum_{j=-\infty}^{\infty} J_j(m\pi\alpha)\, u_{n+j,m} \Bigg], \tag{8.1}$$

where u_{nm} for each n and m is obtained numerically. The time average corresponds to $n = 0$ in the second term:

$$\overline{u'} = \cos kz \sum_{m=+\text{odd}} 2i\sin(m\pi\xi) \sum_{j=-\infty}^{\infty} J_j(m\pi\alpha)\, u_{j,m}. \tag{8.2}$$

Therefore $\overline{u'}$ is odd around the crests ($\xi = 0, \pm 1, \pm 2, \ldots$), and even around the troughs ($\xi = \pm\frac{1}{2}, \pm\frac{3}{2}, \ldots$). The velocity component $\overline{w'}$ can be calculated similarly. To help understand the physical distinctions among the four different types defined in §7, we summarize the odd/even properties of $\overline{u'}$ and $\overline{w'}$ around the crests or the troughs in table 1.

Near the ripple surface η is small, and $\overline{u'}$ and $\overline{w'}$ are dominated by

$$\overline{u'}(\eta) = \left.\frac{\partial \overline{u'}}{\partial \eta}\right|_{\eta=0} \eta + \ldots, \quad \overline{w'}(\eta) = \left.\frac{\partial \overline{w'}}{\partial \eta}\right|_{\eta=0} \eta + \ldots. \tag{8.3}$$

Therefore we only plot the vectors with the components

$$\left.\frac{\partial \overline{u'}}{\partial \eta}\right|_{\eta=0} \quad \text{and} \quad \left.\frac{\partial \overline{w'}}{\partial \eta}\right|_{\eta=0} \tag{8.4}$$

as shown in the lower half of figure 5(*a–k*) for the minimum threshold T and corresponding wavenumber k on the neutral instability curves as indicated in the captions. We have further checked that the flow patterns remain qualitatively

		Crest	Trough
Type I	$\overline{u'}$	odd	even
	$\overline{w'}$	even	odd
Type II	$\overline{u'}$	even	odd
	$\overline{w'}$	odd	even
Type III	$\overline{u'}$	odd	odd
	$\overline{w'}$	even	even
Type IV	$\overline{u'}$	even	even
	$\overline{w'}$	odd	odd

TABLE 1. Parity of the four types of unstable solutions

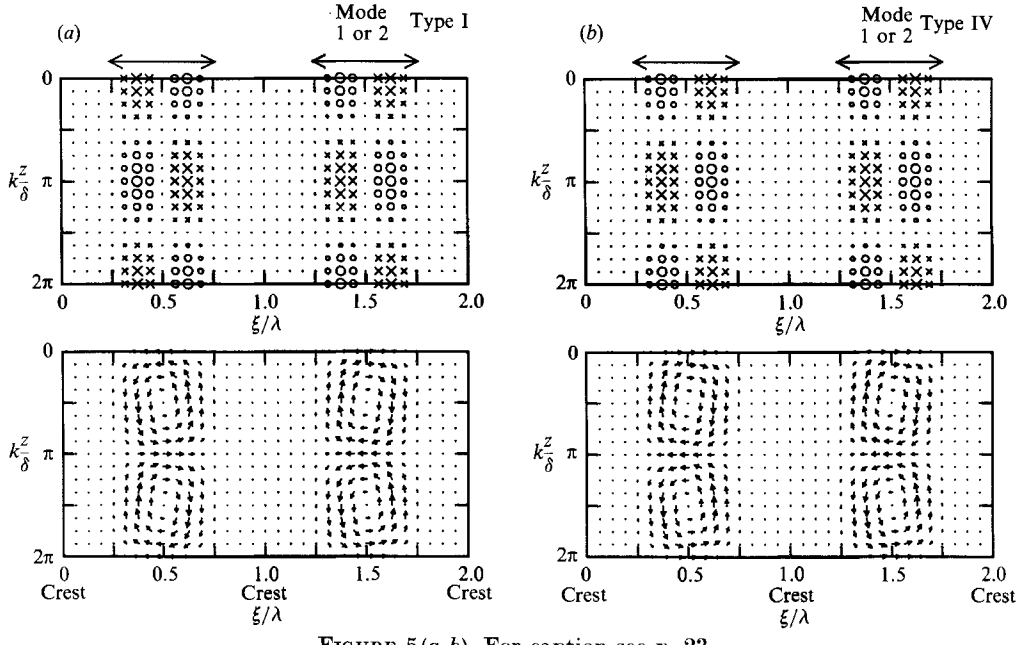

FIGURE 5(a,b). For caption see p. 23.

similar at other points along the same neutral curve. It is on this basis that each neutral instability curve is identified with a mode. Since the absolute magnitude for the eigensolution is arbitrary in the linear theory, the lengths of tangential velocity vectors are normalized by the maximum in each plot, and hence represent the relative magnitude of the local mean velocity. Note that ξ and z in these figures have physical scales and k is the dimensionless wavenumber of the instability threshold.

Also for small but finite η, the velocity divergence in the tangential plane can be used to indicate the tendency of sediment accumulation on the ripple surface. In particular, accumulation may be expected where the divergence is negative. By continuity this divergence is approximately

$$\frac{\partial \overline{u'}}{\partial \xi}+\frac{\partial \overline{w'}}{\partial z}=-\frac{\partial \overline{v'}}{\partial \eta}\approx-\eta\frac{\partial^2 \overline{v'}}{\partial \eta^2}\bigg|_{\eta=0}. \tag{8.5}$$

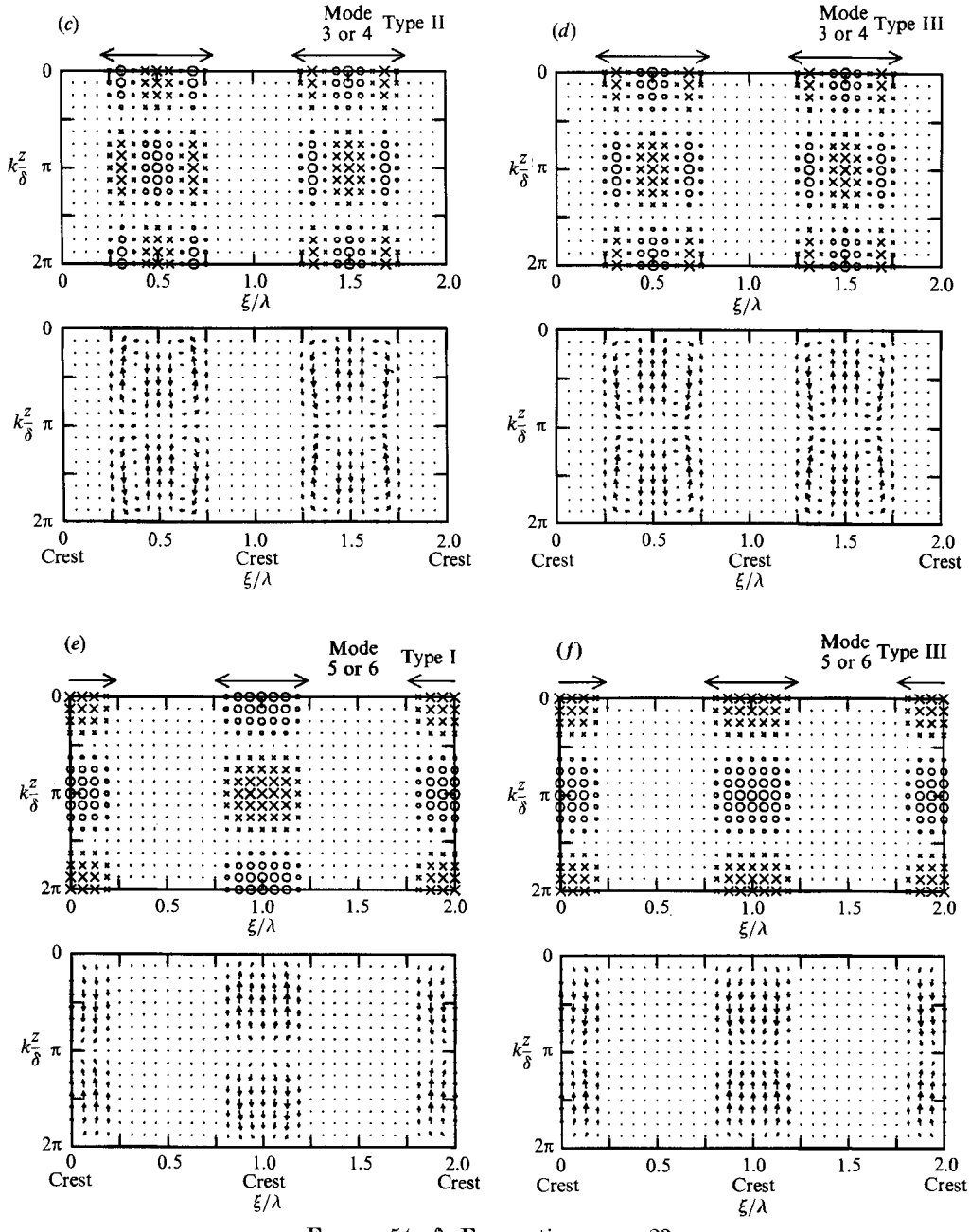

FIGURE 5(*c–f*). For caption see p. 23.

Hence we plot the quantity

$$\left.\frac{\partial^2 \overline{v'}}{\partial \eta^2}\right|_{\eta=0} \tag{8.6}$$

on the upper half of figure 5(*a–k*) for the same thresholds as before. Positive divergence (implying scouring) is shown by × and negative divergence (implying

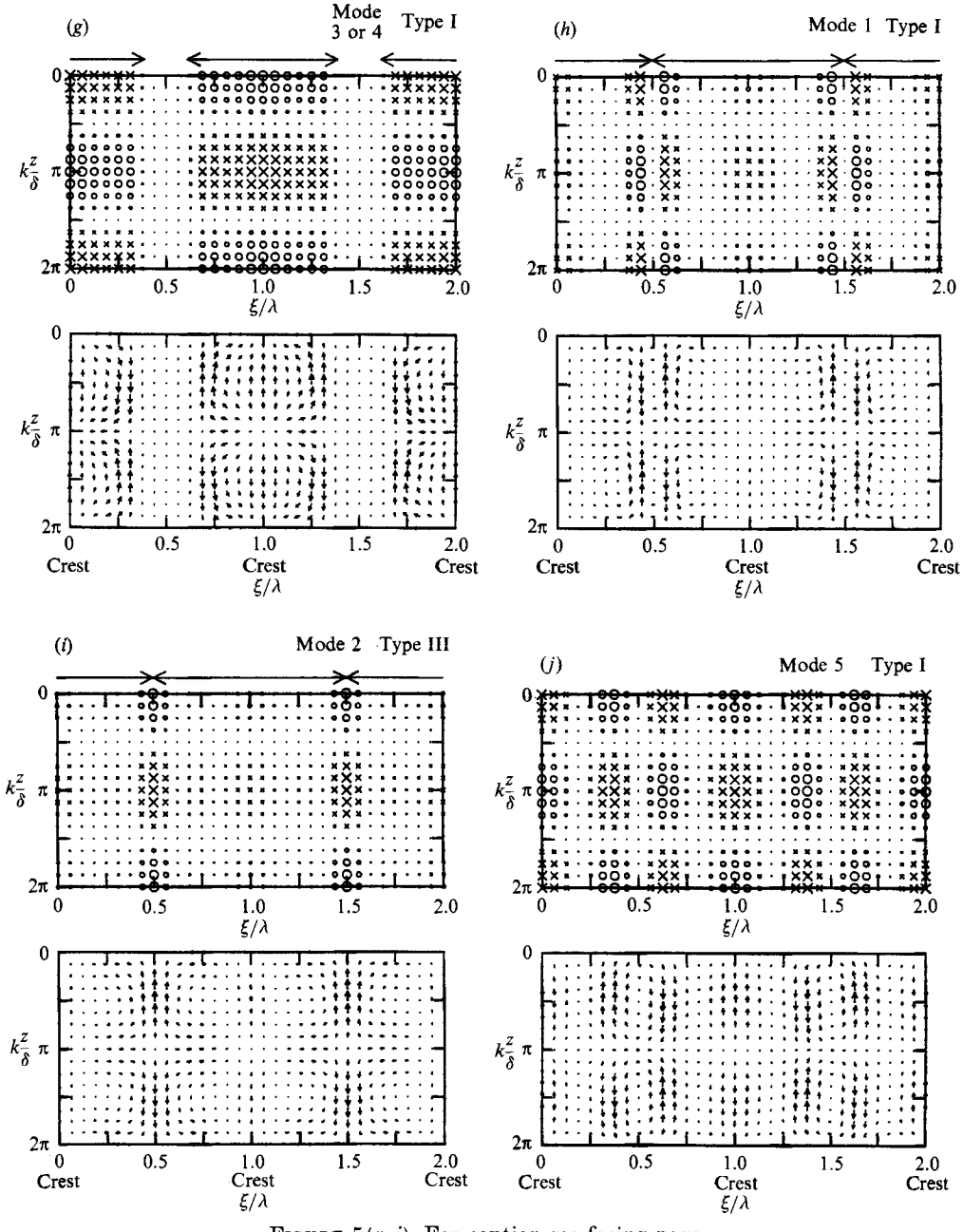

FIGURE 5(*g–j*). For caption see facing page.

accumulation) by ○. The size of each symbol is proportional to the magnitude of the divergence and is normalized again by the maximum in each plot.

As will be discussed in §9, the instability is confined either around the crests or around the troughs for small α. We therefore define the region of influence of the instability by setting as its boundaries where the magnitude of divergence decays to 10% of its maximum. These regions are indicated by arrows above the plots of divergence, for $\alpha = 1/2\pi, 1/\pi$, and modes 1 and 2 of $\alpha = 3/2\pi$.

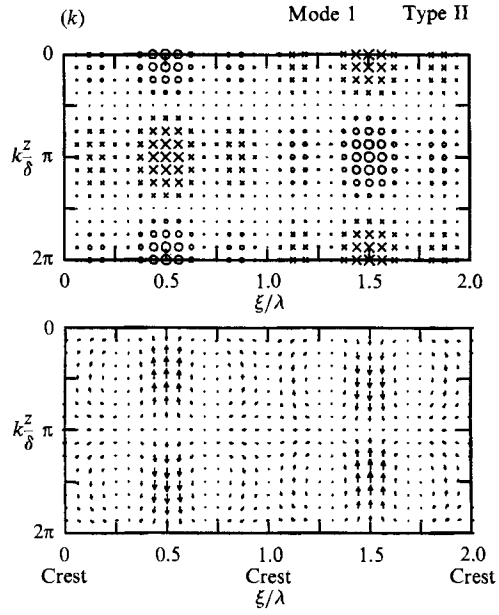

FIGURE 5. Time-averaged tangential velocity field near the ripple surface (bottom figure), and its divergence in the tangential plane (top figure). The magnitudes of velocity and divergence are normalized by the maximum value in each plot. ○, negative divergence; ×, positive divergence. Arrows above the divergence plot indicate region of influence of instability. (*a*) $\alpha = 1/2\pi \approx 0.16$, $k = 0.35$, $T = 0.337$. (*b*) $\alpha = 1/2\pi \approx 0.16$, $k = 0.35$, $T = 0.337$. (*c*) $\alpha = 1/2\pi \approx 0.16$, $k = 0.41$, $T = 0.447$. (*d*) $\alpha = 1/2\pi \approx 0.16$, $k = 0.40$, $T = 0.447$. (*e*) $\alpha = 1/2\pi \approx 0.16$, $k = 0.36$, $T = 0.533$. (*f*) $\alpha = 1/2\pi \approx 0.16$, $k = 0.36$, $T = 0.533$. (*g*) $\alpha = 1/\pi \approx 0.32$, $k = 0.37$, $T = 0.941$. (*h*) $\alpha = 3/2\pi \approx 0.48$, $k = 0.41$, $T = 1.949$. (*i*) $\alpha = 3/2\pi \approx 0.48$, $k = 0.41$, $T = 1.961$. (*j*) $\alpha = 3/2\pi \approx 0.48$, $k = 0.78$, $T = 2.38$. (*k*) $\alpha = 2/\pi \approx 0.64$, $k = 0.52$, $T = 2.06$.

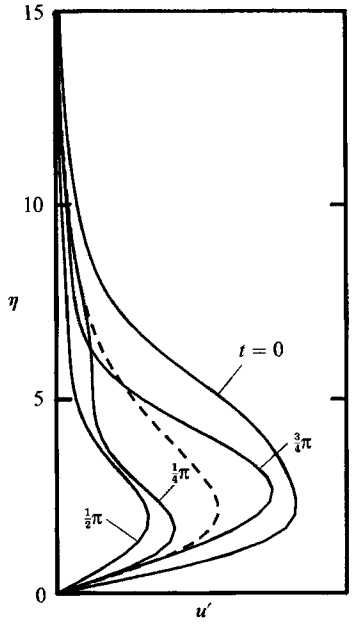

FIGURE 6. Vertical profile of velocity u' at $t = 0, \frac{1}{4}\pi, \frac{1}{2}\pi, \frac{3}{4}\pi$ (solid lines), and its time average (dashed line), at $\xi = 0.5$, $z = 0$, for $\alpha = 1/2\pi \approx 0.16$, mode 1 or 2, Type I.

To give a sample view of the vertical structure of the three-dimensional disturbances we choose to plot in figure 6 the horizontal velocity u' at $z = 0, \xi = \frac{1}{2}$ (trough) for $\alpha = 1/2\pi \approx 0.16$, mode 1 or 2, Type I. Referring to (8.1), the first term in the square bracket is zero at $\xi = \frac{1}{2}$, and u' is periodic in time with a period π. Therefore we plot u' as a function of η at $t = 0, \frac{1}{4}\pi, \frac{1}{2}\pi, \frac{3}{4}\pi$ shown by solid lines, as well as the time average $\overline{u'}$ shown by a dashed line. We now discuss these results for different α.

9. Discussion of results

$\alpha = 1/2\pi \approx 0.16$

This is a case of very weak ambient oscillations. Note from figure 4(*a*) that to the accuracy of our computation (the error is less than 0.5% in the eigenvalue T), two different types of unstable disturbances, one harmonic and one subharmonic, can share the same neutral stability curve. To understand this coincidence of two seemingly different solutions, we compare the flow patterns. From figure 5(*a*) for Type I and 5(*b*) for Type IV, corresponding to modes 1 and 2, we note first that the drift motion is highly localized along the ripple troughs, there being negligible motion along the crests. Therefore the motions along adjacent troughs should be effectively independent of one another, whether the unstable mode is harmonic or subharmonic. Furthermore, the flow patterns along each trough are virtually the same for both types, except for a phase shift of half a wavelength. Between adjacent crests, there appears a single circulation pattern whose direction changes alternately in the z-direction. Because of the absence of interference between adjacent troughs, the phase difference between neighbouring troughs is physically immaterial. In other words, whether the instability belongs to Type I or IV, the flow along each trough is the same. Therefore the coincidence of the neutral instability curves is the consequence of the independence of adjacent troughs and is not surprising.

Consider the next higher modes, 3 and 4, where a subharmonic solution of Type II and a harmonic solution of Type III share the same neutral stability curve, as shown in figure 4(*a*). Again the unstable disturbances are confined to the troughs (figure 5*c*, *d*). Along each trough the flow pattern is much the same. The only distinction between the two types is also a phase shift by half a wavelength. The unstable regions are slightly broader and the flow within each periodic cell shows a double circulation pattern, in contrast to modes 1 and 2.

The first crest instability appears for modes 5 and 6 where Type I (subharmonic) and Type III (harmonic) still share a neutral stability curve. The streaming and divergence patterns clearly suggest that sand may accumulate in checkerboard (figure 5*e*) and rectangular patterns (figure 5*f*).

Note that when the instability is confined around the troughs, the odd/even properties of $\overline{u'}$ and $\overline{w'}$ must be identical at the troughs between the two types sharing the same neutral curve. Referring to table 1, the sharing must be between either Types I and IV or between Types II and III. Similarly for crest instability, possible sharing are Types I and III and Types II and IV.

$\alpha = 1/\pi \approx 0.32$

Modes 1 and 2, 3 and 4, 5 and 6 of $\alpha = 1/\pi$ correspond to modes 1 and 2, 5 and 6, 3 and 4 of $\alpha = 1/2\pi$ respectively, after examining their flow patterns. The features of the streaming and its divergence for $\alpha = 1/\pi$ are qualitatively similar to those for $\alpha = 1/2\pi$, although the unstable region is generally wider. We only show a sample case

of mode 3 or 4, Type I (subharmonic crest instability) in figure 5(*g*). The region of influence is almost twice as wide as the corresponding plot in figure 5(*e*) for $\alpha = 1/2\pi$.

$\alpha = 3/2\pi \approx 0.48$

Here the total displacement amplitude ($2A$) of the ambient oscillation is nearly equal to the ripple wavelength. The neutral instability curves in figure 4(*c*) are the most complex. For modes 1 and 2 the subharmonic (Type I) and harmonic (Type III) disturbances still seem to share the same neutral curves. Both disturbances are unstable at the crest for smaller α. However, the region of instability is now the entire surface, and the flow is no longer confined to the crests (figure 5*h*, *i*). In other words, the disturbances along adjacent crests now interact with one another. Correspondingly there is a slight deviation of the two neutral curves. The same discussion holds for the trough instability modes 3 and 4 and modes 5 and 6. In particular, the flow pattern of mode 5, Type I in figure 5(*j*) shows strong interaction between adjacent troughs and the intensities of disturbances near the crests and near the troughs are comparable. The resulting checkerboard accumulation pattern has a wavelength two-thirds of that of the ripples.

$\alpha = 2/\pi \approx 0.64$

For such strong oscillations the neutral curves of different modes no longer overlap. The interaction between adjacent ripples is significant. Sample velocity and divergence plots are shown in figure 5(*k*) for mode 1, Type II. The accumulation pattern clearly indicates the formation of bridges between transverse crests, which might lead to brick-patterned ripples.

Owing to the high cost of computations, we did not pursue higher values of α.

Since for α less than $1/\pi \approx 0.32$, the instability is localized either along the troughs or the crests, the results should be close to those obtained in §6 for small α when $\epsilon \ll 1$. As a check of computational consistency, we plot in figure 7 the threshold values of T for $\alpha = 1/4\pi, 1/2\pi, 3/4\pi, 1/\pi \approx 0.08, 0.16, 0.24, 0.32$ from the finite-α theory. For $\alpha \to 0$, the threshold Taylor number has been calculated as (6.4) and (6.5) in the limit of small ϵ. These plots can be smoothly interpolated by dashed lines for each mode. In Case (i), we have further pursued a higher-order theory in α. The Taylor number is then expanded as

$$T = T_0 + \alpha T_1 + \ldots, \tag{9.1}$$

where T_0 is the leading-order solution (6.4) or (6.5), and T_1 has multiple eigenvalues. We have only calculated the lowest three values of T_1 for the trough mode and the lowest two values for the crest mode. These results are also shown by solid lines in figure 7. The consistency between the two theories (Cases (i) and (ii)) is evident. We have also determined the spatial variation of the unstable modes along ξ from higher-order theory for Case (i) ($\alpha \ll 1$). The flow field so obtained has been used to compute the steady streaming field for $\alpha = 1/4\pi \approx 0.08$, and is found to be quite consistent with that obtained from the finite-α theory. Since the details do not show further physical insight, the reader is referred to Hara (1990) for further information.

So far no proper experimental results are available for direct comparison with our theory. Matsunaga & Honji (1980) conducted experiments for a vastly different geometry; one of them is cited here for a tentative comparison with our theory. In this experiment, an array of parallel half-circular cylinders (radius $R = 0.70$ cm) were fixed on a flat plate. The spacing between the semicylinders was $\lambda = 2.5$ cm. We use $R/2\lambda = 0.14$ as an estimate for ϵ, which is not at all small. This two-dimensional ripple array was oscillated in calm water with frequency $f = 0.36$ Hz and amplitude

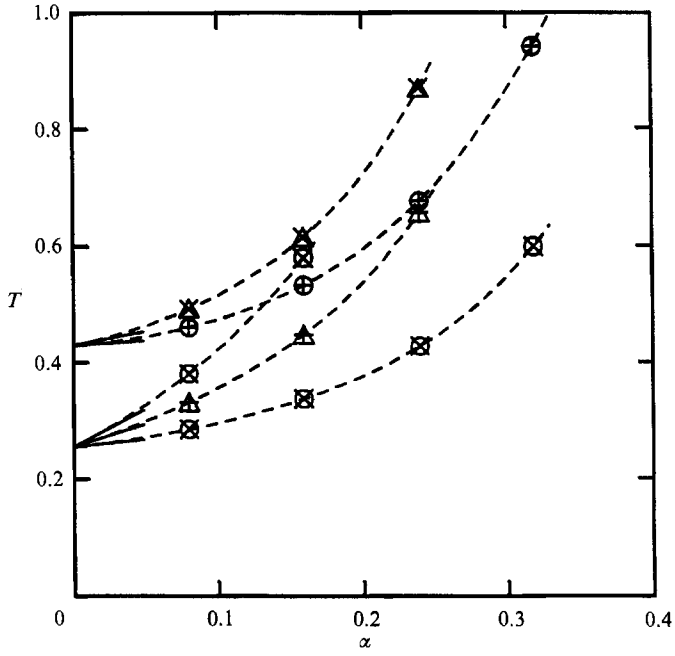

FIGURE 7. Threshold Taylor number T as a function of α. Solid lines are the results for Case (i). Calculated values in Case (ii) are indicated by: ○, Type I; △, Type II; +, Type III; ×, Type IV, and are interpolated by dashed lines.

$A = 0.7$ cm. The parameter $\alpha = A/\lambda = 0.28$ is only moderately large. Water motion was visualized with suspended aluminium flakes, and spanwise periodic streaks in the direction parallel to the oscillation were observed on each cylinder. The positions of streaks on one cylinder were shifted from those on adjacent cylinders by half the spacing, in a form corresponding rather closely to our mode 3 or 4, Type I instability with $\alpha = 1/\pi \approx 0.32$ shown in figure 5 (g). In our theory for small ϵ another harmonic instability of Type III is equally likely. That the latter was not reported is possibly due to the effects of finite ϵ and the circular cylinder geometry which may have caused separation in the basic two-dimensional flow for which our theory is not adequate. Corresponding to the frequency $f = 0.36$ Hz, the Stokes boundary-layer thickness is

$$\delta = \left(\frac{\nu}{\omega}\right)^{\frac{1}{2}} = \left(\frac{\nu}{2\pi f}\right)^{\frac{1}{2}} = 0.066 \text{ cm}, \tag{9.2}$$

where $\nu = 0.01$ cm^2/s, which is the viscosity of water at 20 °C, is used. In our calculation the mode 3 or 4, Type I instability has the largest growth rate around $k = 0.38$; the corresponding wavelength of the instability is

$$\delta \frac{2\pi}{k} = 1.1 \text{ cm}. \tag{9.3}$$

On the other hand, from a photograph in Matsunaga & Honji, the observed wavelength of the instability is roughly 1.7 cm, which is not too different from the theoretical estimate. The quantitative discrepancy can be partly attributed to the difference in geometries. Another possible factor is the water temperature in these experiments, which was not reported. The viscosity of pure water increases by 30%

if the temperature is reduced from 20 °C to 10 °C; the theoretical instability wavelength may then increase by 14%.

From our estimate of ϵ, the Taylor number in the experiment can be calculated as

$$T = \frac{\epsilon\alpha^2}{\sigma} = \frac{0.14 \times 0.28^2}{0.066/2.5} = 0.42, \tag{9.4}$$

which is much lower than the theoretical threshold of modes 3 and 4: $T = 0.94$. This quantitative discrepancy is again likely to be attributable to the significant difference in geometries.

According to figure 4(*b*), modes 1 and 2 (Types I and II) have lower thresholds in T than modes 3 and 4 and instability should be detected first at the troughs and not the crests. However, the trough geometry in their experiments is totally different from being nearly sinusoidal; it is flat (zero curvature) almost everywhere except for the sharp corners where the cylinders intersect the flat bottom. Therefore our predictions for modes 1 and 2 cannot be expected to apply.

Masunaga & Honji performed another experiment with higher frequency $f = 1.8$ Hz and larger amplitude $A = 1.5$ cm. The flow was observed to be turbulent, therefore no comparison with our theory can be made.

Sleath & Ellis (1978) have investigated the formation of ripples by oscillating a sand tray in calm water, with three different particles (medium sand of median diameter 0.40 mm and specific gravity 2.65, silt of median diameter 0.124 mm and specific gravity 2.65, and Perspex grains of media diameter 0.53 mm and specific gravity 1.17). When ripples reached the final equilibrium state, measurements were made of the amplitude and the wavelength of the two-dimensional ripples, as well as the spacing and the height of the bridges, when they were present, between the crests. The ranges of the parameters for which brick-patterned ripples were observed are: $\epsilon = 0.078$–0.139, $\alpha = 0.55$–0.88, and $\sigma = 0.0150$–0.049. Among their records we have found nine cases (all of them with Perspex grains) with α in the range of 0.62–0.66 which is close to our calculations shown in figure 4(*d*) ($\alpha = 0.64$). From their data, the values of ϵ, T and the observed non-dimensional wavenumber k of the three-dimensional bridges are shown in table 2.

According to figure 4(*d*), the least stable mode 1 has the threshold Taylor number $T = 2.06$ with $k = 0.52$ which has only of order-of-magnitude agreement with some of the observations. Despite this quantitative discrepancy, we stress that the theoretical flow structure of mode 1, shown in figure 5(*k*), tends to accumulate particles to form bridges between the ripple crests, and is consistent qualitatively with the observed brick pattern. This suggests, at least tentatively, that the centrifugal instability can be partially responsible for initiating the brick pattern. To achieve a better quantitative agreement, one needs a theory for finite ϵ which accounts for vortex shedding in the basic two-dimensional flow and for the particle motion.

10. Conclusions

We have developed a theory for the three-dimensional instability of centrifugal type of a two-dimensional oscillatory flow over periodic ripples. Under weak ambient oscillations, the least stable mode occurs along the troughs if the ripple slope is sufficiently small. For larger ripple slope, disturbances are first observed along the crests. These disturbances are localized along each ripple, and their mechanism is

Run no.	α	ϵ	T	k
33	0.623	0.112	1.02	0.324
35	0.625	0.104	1.11	0.157
38	0.648	0.085	1.14	0.195
42	0.641	0.120	1.83	0.115
43	0.625	0.100	1.78	0.074
55	0.637	0.107	1.68	0.130
62	0.649	0.108	1.28	0.135
66	0.631	0.118	1.59	0.109
67	0.636	0.106	1.63	0.201

TABLE 2. Measured parameters for brick-patterned ripples in Sleath & Ellis (1978)

similar to that of the spanwise instability along a circular cylinder investigated by Hall.

As the oscillation amplitude increases, the disturbances along adjacent ripples begin to interact with each other, showing more complicated flow patterns of either harmonic or subharmonic type. The associated steady streaming along the ripple surface and its divergence have been calculated. In some cases the flow patterns suggest that centrifugal instability can be relevant to the initiation of brick-patterned ripples, although other factors such as flow–particle interaction and vortex shedding in the basic flow must be effective for the brick pattern to evolve toward final equilibrium.

For quantitative checks on our theory it is certainly desirable to perform controlled experiments with ripples whose shape is close to our theoretical model and with visualization techniques that reveal the flows near the entire ripple surface. On the other hand, further theoretical studies on the instability of oscillatory flows with vortices around steep ripples are worthwhile.

We thank the US Office of Naval Research, Ocean Engineering Program (Contracts N00014-83K 0550 and 89J 3128) and the National Science Foundation, Programs of Fluid Mechanics & Hydraulics and of Ocean Engineering (Grant MSME 8813121) for supporting this research. The relevance of centrifugal instability to brick-patterned ripples was first brought to our attention by Professor A. Kaneko, Kyushu University, in 1986.

Appendix A. The local radius of curvature of the ripple surface

At the ripple surface $\eta = 0$, equation (2.1) becomes

$$x = \xi - a\sin\frac{2\pi\xi}{\lambda}, \quad y = a\cos\frac{2\pi\xi}{\lambda} \tag{A 1}$$

where both x and y are now functions of ξ only. Thus

$$\frac{\mathrm{d}y}{\mathrm{d}x} = \left(\frac{\mathrm{d}y}{\mathrm{d}\xi}\right)\left(\frac{\mathrm{d}x}{\mathrm{d}\xi}\right)^{-1} = \left(-\frac{2\pi a}{\lambda}\sin\frac{2\pi\xi}{\lambda}\right)\left(1-\frac{2\pi a}{\lambda}\cos\frac{2\pi\xi}{\lambda}\right)^{-1} \tag{A 2}$$

and

$$\frac{\mathrm{d}^2y}{\mathrm{d}x^2} = \left(\frac{\mathrm{d}x\,\mathrm{d}^2y}{\mathrm{d}\xi\,\mathrm{d}\xi^2} - \frac{\mathrm{d}^2x\,\mathrm{d}y}{\mathrm{d}\xi^2\,\mathrm{d}\xi}\right)\left(\frac{\mathrm{d}x}{\mathrm{d}\xi}\right)^{-3} = \left[\left(1-\frac{2\pi a}{\lambda}\cos\frac{2\pi\xi}{\lambda}\right)\left(-\frac{4\pi^2 a}{\lambda^2}\cos\frac{2\pi\xi}{\lambda}\right) - \left(\frac{4\pi^2 a}{\lambda^2}\sin\frac{2\pi\xi}{\lambda}\right)\left(-\frac{2\pi a}{\lambda}\sin\frac{2\pi\xi}{\lambda}\right)\right]\left(1-\frac{2\pi a}{\lambda}\cos\frac{2\pi\xi}{\lambda}\right)^{-3}$$

$$= \frac{4\pi^2 a}{\lambda^2}\left(\frac{2\pi a}{\lambda} - \cos\frac{2\pi\xi}{\lambda}\right)\left(1-\frac{2\pi a}{\lambda}\cos\frac{2\pi\xi}{\lambda}\right)^{-3}. \tag{A 3}$$

The local radius of curvature is, by definition,

$$R_{\mathrm{L}} = \left\{-\frac{\mathrm{d}^2y}{\mathrm{d}x^2}\left[1+\left(\frac{\mathrm{d}y}{\mathrm{d}x}\right)^2\right]^{-\frac{3}{2}}\right\}^{-1} = \frac{\lambda^2}{4\pi^2 a}\left(1-\frac{2\pi a}{\lambda}\cos\frac{2\pi\xi}{\lambda}\right)^3\left(\cos\frac{2\pi\xi}{\lambda}-\frac{2\pi a}{\lambda}\right)^{-1} \times\left\{1+\left[\left(-\frac{2\pi a}{\lambda}\sin\frac{2\pi\xi}{\lambda}\right)\left(1-\frac{2\pi a}{\lambda}\cos\frac{2\pi\xi}{\lambda}\right)^{-1}\right]^2\right\}^{\frac{3}{2}}$$

$$= \frac{\lambda^2}{4\pi^2 a}\left[1-2\frac{2\pi a}{\lambda}\cos\frac{2\pi\xi}{\lambda}+\left(\frac{2\pi a}{\lambda}\right)^2\right]^{\frac{3}{2}}\left(\cos\frac{2\pi\xi}{\lambda}-\frac{2\pi a}{\lambda}\right)^{-1}. \tag{A 4}$$

After normalization,

$$R_{\mathrm{L}} = \frac{\lambda^2}{4\pi^2 a}\frac{[1-4\pi\epsilon\cos(2\pi\xi)+4\pi^2\epsilon^2]^{\frac{3}{2}}}{[\cos(2\pi\xi)-2\pi\epsilon]} = \frac{\lambda^2}{4\pi^2 a}\frac{J^{\frac{3}{2}}}{[\cos(2\pi\xi)-2\pi\epsilon^2]}. \tag{A 5}$$

Appendix B. Numerical procedure for solving the eigenvalue problem

In §7 we have obtained coupled ordinary differential equations (7.18) and (7.19) governing u_{nm} and v_{nm} with boundary conditions (7.20).

We first seek neutrally stable solutions of eigen functions u_{nm}, v_{nm} and eigenvalue T for given k, setting $s = 0$. The numerical method by Hall (1984), which involves only one summation, may be readily extended for two summations. Specifically, for $\eta > \eta_M$ where η_M is a large enough value, we can approximate (7.18) and (7.19) by neglecting coefficients which decay exponentially,

$$\left(\frac{\partial^2}{\partial\eta^2}-k^2-\mathrm{i}n\right)u_{nm} = 0, \tag{B 1}$$

$$\left(\frac{\partial^2}{\partial\eta^2}-k^2-\mathrm{i}n\right)\left(\frac{\partial^2}{\partial\eta^2}-k^2\right)v_{nm} - 2\pi^2k^2\frac{T}{\alpha}\sum_{j=-\infty}^{\infty}[J_{j-1}(2\pi\alpha)+J_{j+1}(2\pi\alpha)][u_{n-j,m-2}-(-1)^j u_{n-j,m+2}] = 0. \tag{B 2}$$

The solutions of the uncoupled ordinary differential equations (B 1) which satisfy the boundary conditions (7.20) at $\eta = \infty$ are

$$u_{nm} = a_{nm}\exp[-(k^2+\mathrm{i}n)^{\frac{1}{2}}\eta]. \tag{B 3}$$

From (B 2) we get for $n \neq 0$,

$$v_{nm} = \sum_{j\neq 0,\, n} 2\pi^2 k^2 \frac{T}{\alpha}[J_{j-1}(2\pi\alpha)+J_{j+1}(2\pi\alpha)][a_{n-j,\,m-2}-(-1)^j a_{n-j,\,m+2}]$$
$$\times \frac{1}{j(n-j)}\exp[-(k^2+\mathrm{i}(n-j))^{\frac{1}{2}}\eta]$$
$$+ 2\pi^2 k^2 \frac{T}{\alpha}[J_{n-1}(2\pi\alpha)+J_{n+1}(2\pi\alpha)][a_{0,\,m-2}-(-1)^n a_{0,\,m+2}]\frac{1}{2\mathrm{i}kn}\eta\, \mathrm{e}^{-k\eta}$$
$$+ b_{nm}\,\mathrm{e}^{-k\eta}+c_{nm}\exp[-(k^2+\mathrm{i}n)^{\frac{1}{2}}\eta]. \tag{B 4a}$$

When $n = 0$, v_{nm} is replaced by

$$v_{0m} = -\sum_{j\neq 0} 2\pi^2 k^2 \frac{T}{\alpha}[J_{j-1}(2\pi\alpha)+J_{j+1}(2\pi\alpha)][a_{-j,\,m-2}-(-1)^j a_{-j,\,m+2}]$$
$$\times \frac{1}{j^2}\exp[-(k^2-ij)^{\frac{1}{2}}\eta]+b_{0m}\,\mathrm{e}^{-k\eta}+c_{0m}\,\eta\,\mathrm{e}^{-k\eta}. \tag{B 4b}$$

For brevity, we only show the numerical procedure for Type I. That for the other three Types has been carried out similarly.

We truncate the Fourier series (7.16) at $n = \pm N$ and $m = \pm M$. In view of (7.17) and (7.26) the coefficients a_{nm}, b_{nm}, c_{nm} must satisfy

$$\left.\begin{aligned} a^*_{nm} &= a_{-n,-m} = (-1)^{n+1} a_{-n,m},\\ b^*_{nm} &= b_{-n,-m} = (-1)^n b_{-n,m},\\ c^*_{nm} &= c_{-n,-m} = (-1)^n c_{-n,m}. \end{aligned}\right\} \tag{B 5}$$

In particular for $n = 0$

$$a^*_{0m} = a_{0,-m} = -a_{0m}, \quad b^*_{0m} = b_{0,-m} = b_{0m}, \quad c^*_{0m} = c_{0,-m} = c_{0m}, \tag{B 6}$$

which indicates that a_{0m} is purely imaginary while b_{0m} and c_{0m} are real. In setting

$$a_{nm} = a^{\mathrm{r}}_{nm} + \mathrm{i}a^{\mathrm{i}}_{nm}, \quad b_{nm} = b^{\mathrm{r}}_{nm} + \mathrm{i}b^{\mathrm{i}}_{nm}, \quad c_{nm} = c^{\mathrm{r}}_{nm} + \mathrm{i}c^{\mathrm{i}}_{nm}, \tag{B 7}$$

where a^{r}_{nm}, a^{i}_{nm}, b^{r}_{nm}, b^{i}_{nm}, c^{r}_{nm}, c^{i}_{nm} are real, we may identify the following $\frac{1}{2}(6N+3)(M+1)$ independent real coefficients:

$$\left.\begin{aligned} a^{\mathrm{r}}_{nm} \quad & n = 1\text{–}N\\ a^{\mathrm{i}}_{nm} \quad & n = 0\text{–}N\\ b^{\mathrm{r}}_{nm}, c^{\mathrm{r}}_{nm} \quad & n = 0\text{–}N\\ b^{\mathrm{i}}_{nm}, c^{\mathrm{i}}_{nm} \quad & n = 1\text{–}N \end{aligned}\right\} \quad m = 1, 3, \ldots, M. \tag{B 8}$$

We now set one of these coefficients to be 1 and all the others to be 0, and calculate the values of u_{nm}, v_{nm} and their derivatives at $\eta = \eta_M$. Using these as the initial conditions, we integrate the unapproximated equations (7.18) and (7.19) from $\eta = \eta_M$ to $\eta = 0$ by a fourth-order Runge–Kutta scheme. After repeating this procedure for all the coefficients, the solutions of u_{nm} and v_{nm} can be written as the linear combination of these $\frac{1}{2}(6N+3)(M+1)$ independent solutions. The coefficients are then determined so that the boundary conditions (7.20) are satisfied at $\eta = 0$, as follows.

Recall that u_{nm} and v_{nm} satisfy (7.17) and (7.26), i.e.

$$u^*_{nm} = u_{-n,-m} = (-1)^{n+1} u_{-n,m}, \quad v^*_{nm} = v_{-n,-m} = (-1)^n v_{-n,m} \tag{B 9}$$

In particular, u_{0m} is purely imaginary and v_{0m} is real. If we set

$$u_{nm} = u^{\mathrm{r}}_{nm} + \mathrm{i}u^{\mathrm{i}}_{nm}, \quad v_{nm} = v^{\mathrm{r}}_{nm} + \mathrm{i}v^{\mathrm{i}}_{nm}, \tag{B 10}$$

where $u^{\mathrm{r}}_{nm}, u^{\mathrm{i}}_{nm}, v^{\mathrm{r}}_{nm}, v^{\mathrm{i}}_{nm}$ are real, the boundary conditions (7.20) at $\eta = 0$ yield

$$\left.\begin{aligned} u^{\mathrm{r}}_{nm} &= 0 \quad n = 1\text{–}N \\ u^{\mathrm{i}}_{nm} &= 0 \quad n = 0\text{–}N \\ v^{\mathrm{r}}_{nm} = \frac{\mathrm{d}v^{\mathrm{r}}_{nm}}{\mathrm{d}\eta} &= 0 \quad n = 0\text{–}N \\ v^{\mathrm{i}}_{nm} = \frac{\mathrm{d}v^{\mathrm{i}}_{nm}}{\mathrm{d}\eta} &= 0 \quad n = 1\text{–}N \end{aligned}\right\} \quad m = 1, 3, \ldots, M \quad \text{at } \eta = 0, \tag{B 11}$$

which provides $\frac{1}{2}(6N+3)(M+1)$ conditions to determine equal number of real coefficients.

For non-neutral modes, $s \neq 0$, the approximate equations for $\eta > \eta_M$ are modified as

$$\left(\frac{\partial^2}{\partial\eta^2} - k^2 - \mathrm{i}n - s\right) u_{nm} = 0 \tag{B 12}$$

$$\left(\frac{\partial^2}{\partial\eta^2} - k^2 - \mathrm{i}n - s\right)\left(\frac{\partial^2}{\partial\eta^2} - k^2\right) v_{nm}$$

$$- 2\pi^2 k^2 \sum_{j=-\infty}^{\infty} [J_{j-1}(2\pi\alpha) + J_{j+1}(2\pi\alpha)][u_{n-j,m-2} - (-1)^j u_{n-j,m+2}] = 0, \tag{B 13}$$

and the solutions as

$$u_{nm} = a_{nm} \exp[-(k^2 + \mathrm{i}n + s)^{\frac{1}{2}}\eta], \tag{B 14}$$

$$v_{nm} = \sum_{j\neq 0} 2\pi^2 k^2 \frac{T}{\alpha} [J_{j-1}(2\pi\alpha) + J_{j+1}(2\pi\alpha)][a_{n-j,m-2} - (-1)^j a_{n-j,m+2}]$$

$$\times \frac{1}{-[\mathrm{i}(n-j)+s]\,\mathrm{i}j} \exp[-(k^2 + \mathrm{i}(n-j) + s)^{\frac{1}{2}}\eta]$$

$$+ b_{nm}\,\mathrm{e}^{-k\eta} + c_{nm} \exp[-(k^2 + \mathrm{i}n + s)^{\frac{1}{2}}\eta]. \tag{B 15}$$

By prescribing s and k, the eigenvalue T can be calculated with the eigenfunctions u_{nm} and v_{nm} as in the case of neutral instability.

In each calculation of the eigenvalue T, we increased N, M and η_M and decreased $\Delta\eta$ until the solution converged. The range of values of N and M are shown in table 3. As α increases, more time harmonics (greater N) are required. On the other hand, the number M of the spatial harmonics is greater for smaller α since the instability is confined in a narrower region around the crest/trough as was already discussed in §6. In all the calculations, we used $\eta_M = 15.0$, $\Delta\eta = 0.33$ or 0.5. With these values, the errors of the eigenvalue T are at most 0.5%. In the calculation of velocity fields, it was necessary to include 2 or 3 more spatial harmonics to obtain 1% accuracy.

Calculations were carried out on the Cray X-MP super computers at Pittsburgh Supercomputing Center and at the Naval Research Laboratory in Washington, DC. Typical CPU time for one eigenvalue T was 400 s for $N = 11$, $M = 9$ or 80 s for $N =$

α	N	M
$1/2\pi \approx 0.16$	3–5	10–15
$1/\pi \approx 0.32$	6–7	8–12
$3/2\pi \approx 0.48$	7–9	6–12
$2/\pi \approx 0.64$	10–11	6–9

TABLE 3. Numbers of time (N) and space (M) harmonics

7, $M = 6$. We have also tried to calculate for $\alpha = 5/2\pi \approx 0.80$, but the computation was too costly for us to pursue.

REFERENCES

ABRAMOWITZ, M. & STEGUN, I. A. 1965 *Handbook of Mathematical Functions*. Dover.

BAGNOLD, R. A. 1946 Motion of waves in shallow water; interaction between waves and sand bottoms. *Proc. R. Soc. Lond.* A **187**, 1–15.

BATCHELOR, G. K. 1967 *An introduction to Fluid Mechanics*. Cambridge University Press.

BENJAMIN, T. B. 1959 Shearing flow over a wavy boundary. *J. Fluid Mech.* **6**, 161–205.

DAVIS, S. H. 1976 The stability of time-periodic flows. *Ann. Rev. Fluid Mech.* **8**, 57–74.

HALL, P. 1984 On the stability of the unsteady boundary layer on a cylinder oscillating transversely in a viscous fluid. *J. Fluid Mech.* **146**, 347–367.

HARA, T. 1990 Nonlinear dynamics near a wavy boundary on the sea surface or the sea bottom. Ph.D. thesis, MIT.

HARA, T. & MEI, C. C. 1990 Oscillating flows over periodic ripples. *J. Fluid Mech.* **211**, 183–209.

HONJI, H. 1981 Streaked flow around an oscillating circular cylinder. *J. Fluid Mech.* **107**, 509–520.

KANEKO, A. & HONJI, H. 1979 Double structures of steady streaming in the oscillatory viscous flow over a wavy wall. *J. Fluid Mech.* **93**, 727–736.

KERCZEK, C. VON & DAVIS, S. H. 1974 Linear stability theory of oscillatory Stokes layer. *J. Fluid Mech.* **62**, 753–773.

LI, H. 1954 Stability of oscillatory laminar flow along a wall. *Beach Erosion Board, US Army Corps Engng, Wasington DC, Tech. Memo*, 47.

LYNE, W. H. 1971 Unsteady viscous flow over a wavy wall. *J. Fluid Mech.* **50**, 33–48.

MATSUNAGA, N. & HONJI, H. 1980 Formation mechanism of brick-pattern ripples. *Rep. Res. Inst. Appl. Mech., Kyushu Univ.*, vol. 28, no. 88, pp. 27–38.

SARPKAYA, T. 1986 Force on a circular cylinder in viscous oscillatory flow at low Keulegan–Carpenter numbers. *J. Fluid Mech.* **165**, 61–71.

SERGEEV, S. I. 1966 Fluid oscillations in pipes at moderate Reynolds numbers. *Mekh. Zhidk. Gaza* **1**, no. 1, 168–170. (Transl. in *Fluid Dyn.* **1**, no. 1, 121–122.)

SLEATH, J. F. A. 1984 *Sea Bed Mechanics*. Wiley-Interscience.

SLEATH, J. F. A. & ELLIS, A. C. 1978 Ripple geometry in oscillatory flow. *University of Cambridge. Dept. of Engng Rep.* A/Hydraul./TR2.

THOMPSON, C. 1987 Stability of a Stokes boundary layer. *J. Acoust. Soc. Am.* **81**, 861–873.

VITTORI, G. 1989 Non-linear viscous oscillatory flow over a small amplitude wavy wall. *J. Hydraul. Res.* **27**, 267–280.

YIH, C. S. 1968 Instability of unsteady flows or configurations. Part 1. Instability of a horizontal liquid layer on an oscillating plane. *J. Fluid Mech.* **31**, 737–751.